Infection and Drug Resistance

Dovepress
Taylor & Francis Group

Open Access Full Text Article

ORIGINAL RESEARCH

Hydroxysafflor Yellow A Mitigates Sepsis-Induced Pulmonary and Intestinal Injury by Inhibiting TP53 Mediated Ferroptosis

Qing Chen[1,*], Chencheng Xu[1,2,*], Jinzhong Fei[3,*], Zhengbin Wu[1], Yaoli Wang[1], Yingjie Wang[3], Shifeng Shao[1]

[1]Department of ICU, Daping Hospital, Army Medical University, Chongqing, 400042, People's Republic of China; [2]The 955 Hospital of the Chinese People's Liberation Army Ground Force, Changdu, 854000, People's Republic of China; [3]Department of Post-Graduate School, Army Medical University, Chongqing, 400042, People's Republic of China

*These authors contributed equally to this work

Correspondence: Yingjie Wang, Department of Post-Graduate School, Army Medical University, Chongqing, 400042, People's Republic of China, Email yingjiewang@tmmu.edu.cn; Shifeng Shao, Department of ICU, Daping Hospital, Army Medical University, Chongqing, 400042, People's Republic of China, Email shaosf@tmmu.edu.cn

Introduction: Sepsis is a common and life-threatening condition in clinical practice, leading to mortality among intensive care unit (ICU) patients. Due to its unclear pathogenesis, underscoring the urgent need for effective therapeutic strategies. Ferroptosis plays a pivotal role in sepsis progression, and ferroptosis-related genes represent promising intervention targets.

Methods: This study performed bioinformatics to identify ferroptosis-related hub genes in sepsis. We used septic mice and lipopolysaccharide (LPS)-treated IECs to detected the role of TP53-mediated ferroptosis in sepsis. Furthermore, in vitro and in vivo experiments were conducted to validate the effect of hydroxysafflor yellow A (HSYA) on TP53-mediated ferroptosis and sepsis.

Results: TP53 has been identified as a ferroptosis-related hub gene in sepsis. Inhibition of TP53 with the specific TP53 inhibitor Pifithrin-α markedly reduced ferroptosis both in vitro and in vivo. Meanwhile, inhibition of TP53 significantly reduced inflammation and improved sepsis-induced intestinal barrier dysfunction. Furthermore, this study found that HSAY, a core component of XueBiJing, could stably bind to TP53, reduced the expression of TP53 and TP53-mediated ferroptosis in sepsis and improved animal survival.

Conclusion: This study clarified the role of TP53-mediated ferroptosis in sepsis-induced intestinal barrier dysfunction and discovered that HSYA could improve sepsis as an inhibitor of TP53, offering new strategies for the treatment of sepsis.

Keywords: sepsis, TP53, ferroptosis, acute lung injury, intestinal barrier dysfunction

Introduction

Sepsis is a life-threatening organ dysfunction caused by a dysregulated host response to infection.[1] Without timely and effective intervention, the mortality rate can rapidly exceed 30–35%.[2] Globally, sepsis accounts for 11 million deaths annually, representing one-fifth of all causes of death. Severe and critical viral sepsis induced by coronavirus disease (COVID-19) has resulted in app roximately six million deaths worldwide to date. These statistics indicate that sepsis imposes a substantial burden on healthcare systems and remains a major challenge in modern medicine.[3] Pulmonary and intestinal dysfunction are the most common forms of organ failure in sepsis. Studies have shown that nearly 50% of patients with sepsis in intensive care units develop intestinal injury, which is closely associated with the occurrence of septic shock and 28-day mortality.[4] Epidemiological data further reveal that over 210,000 sepsis cases are diagnosed annually in the United States, with 50% of patients experiencing sepsis-induced lung injury, leading to poor prognosis.[5]

When the inflammatory response and organ injury in sepsis intensify, the condition may progress to septic shock, a critical state marked by profound circulatory disturbance and cellular metabolic abnormalities. The core mechanism is refractory hypotension driven by the inflammatory cascade of sepsis, persisting despite adequate fluid resuscitation.[6] In

Received: 17 August 2025
Accepted: 2 December 2025
Published: 8 December 2025

this stage, the intestine and lung, as the two major barrier organs in closest contact with the external environment, are often the earliest targets of damage. Their injury rapidly deteriorates due to the combined effects of insufficient perfusion and inflammatory insult.[7,8] Under ischemic and hypoxic stress, the body initiates blood redistribution, diverting flow from the gastrointestinal tract, kidneys, skeletal muscles, and skin toward vital organs such as the brain and heart to preserve perfusion. Although this compensatory process sustains critical organ function, it induces intestinal hypoperfusion. In this state, the intestinal mucosa exhibits pathological alterations, including enhanced microbial virulence, suppression of epithelial cell proliferation, and downregulation of tight junction proteins, ultimately compromising barrier integrity.[9] Barrier collapse allows bacteria and endotoxins to translocate, triggering excessive activation of the systemic immune system, particularly the monocyte–macrophage system, and inducing massive cytokine and inflammatory mediator release. The resulting uncontrolled systemic inflammation can escalate to multiple organ dysfunction syndrome (MODS).[10,11] At this point, the continuous influx of bacteria and toxins into the circulation acts as a persistent "fuel" for inflammation, establishing the intestine as a key driver of post-sepsis organ dysfunction.[12] Sepsis-induced acute lung injury frequently serves as an early initiating event. Microcirculatory disturbances and hypoxia exacerbate injury to alveolar epithelial and vascular endothelial cells, resulting in increased exudation into the alveolar space and severe impairment of gas exchange. The pathogenesis involves multiple interconnected mechanisms, including aberrant immune cell activation, apoptosis, oxidative stress, heightened vascular permeability, and excessive release of inflammatory mediators. Dysregulated host responses to these mediators amplify the inflammatory cascade, aggravating lung injury and ultimately progressing to acute respiratory distress syndrome (ARDS),[13,14] thereby establishing a lethal "shock–hypoxia–organ injury" cycle. Despite the high incidence and clinical severity of sepsis-induced intestinal and pulmonary injury, effective targeted therapeutic or protective interventions remain unavailable. Standard clinical approaches, such as lung-protective ventilation and fluid resuscitation, fail to halt the inflammatory cascade. Elucidation of the molecular pathways underlying post-sepsis organ injury, coupled with the identification of protective and therapeutic strategies targeting both the lung and intestine, is essential to overcoming therapeutic limitations and improving clinical outcomes in sepsis.

Ferroptosis is a unique form of programmed cell death, distinct from apoptosis, that is iron-dependent and characterized by excessive lipid peroxide accumulation, leading to disruption of cell membrane integrity and eventual cell death.[15] *GPX4* mitigates oxidative stress by reducing lipid hydroperoxides to non-toxic lipid alcohols, and its pivotal role in this process makes it a widely accepted marker of ferroptosis. Ferroptosis has been implicated in a broad spectrum of diseases. Disruption of redox homeostasis by factors such as infection or cancer can trigger ferroptosis, accelerating pathological progression and resulting in adverse clinical outcomes.[16–18] Targeted modulation of ferroptosis has demonstrated therapeutic potential in conditions including tumor metastasis, ischemia–reperfusion injury, and sepsis. Growing evidence highlights a crucial role for ferroptosis in sepsis.[19] Zhang et al found that *YAP1* inhibits ferroptosis by suppressing ferritinophagy. Conditional knockout of *YAP1* in pulmonary epithelial cells aggravated acute lung injury and enhanced pulmonary ferroptosis in septic mice.[20]

Tang et al demonstrated that *AUF1* inhibits ferroptosis by upregulating *NRF2* and downregulating *ATF3*. Deletion of the *AUF1* gene exacerbated acute lung injury in septic mice, reduced survival rates, and promoted the onset and progression of pulmonary ferroptosis.[21] During sepsis, ferroptosis can facilitate infection by supplying essential substrates for bacterial proliferation. Immune cells may undergo ferroptosis, leading to reductions in both number and function. Ferroptotic cells can be recognized by immune cells, initiating a series of inflammatory or antigen-specific immune responses. These processes compromise host immunity, potentially induce autoimmunity, and lead to immune dysfunction, thereby aggravating infection and driving the progression to sepsis and subsequent development of MODS.[22–25]

XueBiJing (XBJ), an injectable formulation comprising five medicinal herbs, has been integrated into routine clinical management of sepsis in China.[26] Its major active constituents, including HSYA, paeoniflorin, albiflorin, and tanshinol, exhibit significant anti-septic activities such as modulating immune responses, suppressing excessive inflammation, regulating hemostasis, and improving organ function.[27] Clinical studies have confirmed the therapeutic efficacy of XBJ in patients with sepsis. Qiu et al reported that intravenous infusion of 100 mL XBJ every 12 hours for five consecutive days in 1,817 patients significantly reduced the 28-day mortality rate compared with placebo, with a slightly lower incidence

of adverse events in the XBJ group.[28] Preclinical studies have further demonstrated that XBJ improves the symptoms of sepsis-induced acute lung injury by mitigating oxidative stress and ferroptosis.[29] HSYA, one of the principal components of XBJ, has been shown to prevent cardiovascular and cerebral ischemia–reperfusion injury through antioxidant, anti-inflammatory, and neuroprotective effects.[30] Recently, Deng X and colleagues found in a murine model of sepsis-induced lung injury that HSYA alleviates pulmonary injury and inflammation.[31] Based on the core antioxidant and anti-inflammatory properties of HSYA confirmed by previous studies, and considering that its potential targets (eg, Nrf2, GPX4) are key regulators of the ferroptosis pathway.[32,33] We hypothesize that HSYA may exert a therapeutic effect on sepsis by regulating the ferroptosis mechanism.

To test the proposed hypothesis, bioinformatics analysis was conducted using the R software environment and the limma package on three Gene Expression Omnibus (GEO) datasets (GSE28750, GSE57065, and GSE95233). The analysis aimed to identify DEGs and key hub genes involved in the ferroptosis pathway in sepsis. Guided by these findings, a cecal ligation and puncture (CLP) mouse model of sepsis was established to experimentally assess the role of the *TP53* gene. Molecular docking analysis was subsequently performed to examine the binding specificity between HSYA and *TP53*. To further validate the predictions, both in vivo and in vitro experiments were conducted.

Materials and Methods

Identification of Ferroptosis-Related Genes

Ferroptosis-related genes were obtained from the GeneCards and FerrDb databases. Three sepsis-related microarray datasets (GSE28750, GSE57065, and GSE95233) were retrieved from the GEO database for analysis. Data processing and analysis were performed using R software (version 4.1.2). Based on the platform annotation files, probe identifiers in the gene expression profiles were converted into corresponding gene symbols. DEGs were identified using the limma package, with thresholds set at $p < 0.05$ and $|\log_2$ fold change (logFC)$| > 0.8$. Key ferroptosis-related DEGs were determined using Venn diagram analysis.

Construction of an Artificial Neural Network Model

Initially, genes were scored based on their regulation patterns, with upregulated and downregulated genes scored separately. Genes with an absolute $\log_2$ fold change (|logFC|) greater than the median |logFC| across all genes in the dataset were assigned a score of 1, whereas all other genes were assigned a score of 0. A total of 30% of the samples were randomly selected as the validation set, and the remaining 70% were used as the training set. The training set was employed to optimize the weights of the candidate differentially expressed genes, while the validation set was used to evaluate the classification performance of the model.

Single-Cell RNA-Seq Data

The single-cell RNA-seq dataset GSE175453, related to sepsis, was downloaded from the Gene Expression Omnibus (GEO) database. Data processing and analysis were performed using the Seurat package (v5.0.1) in R. The raw gene expression matrix was read using the Read10X function and initialized as a Seurat object with CreateSeuratObject. Quality control was applied to remove low-quality cells: we retained genes detected in at least 3 cells, and then filtered out cells meeting any of the following criteria: 1) mitochondrial gene percentage > 20%; 2) hemoglobin gene (indicative of red blood cells) percentage > 1%; 3) the number of detected genes per cell was higher than the 99th percentile of the distribution (to exclude potential doublets). Following QC, gene expression counts were normalized using the LogNormalize method. The top 2000 highly variable genes were identified using FindVariableFeatures and subsequently scaled using ScaleData. Dimensionality reduction was performed using principal component analysis (PCA). Cells were clustered based on the top principal components with the FindNeighbors and FindClusters functions. Differentially expressed genes for each cluster were identified using FindAllMarkers, with thresholds set at $|\log_2$ fold change$| > 0.25$ and expression in a minimum of 25% of cells within the cluster of interest. Finally, cell clusters were annotated by integrating the identified marker genes with well-established cell-type markers from the literature.

Functional Enrichment and PPI Network Analysis

Sepsis samples from GSE28750, GSE57065, and GSE95233 were stratified into high and low TP53 expression groups. In each group, differentially expressed ferroptosis-related genes were identified using the same procedures and parameters described above. Functional enrichment analyses, including Gene Ontology (GO), Kyoto Encyclopedia of Genes and Genomes (KEGG) pathway analysis, and gene set enrichment analysis (GSEA), were conducted with the clusterProfiler package. Protein–protein interaction (PPI) networks were generated using the STRING database with a minimum interaction score threshold of >0.4. Network visualization and hub gene identification were performed in Cytoscape 3.6.1 using the Degree algorithm.

Consensus Clustering Analysis

Consensus clustering was conducted using the ConsensusClusterPlus package, with 5,000 iterations to minimize the randomness of K-means clustering and enhance cluster stability. K-means clustering inertia was calculated as the sum of the mean squared distances between each sample and its nearest cluster centroid.

Immune-Related Analysis

Immune-related genes were retrieved from the ImmPort database, and intergroup differences were analyzed to define immune phenotypes. Single-sample gene set enrichment analysis (ssGSEA) was performed using the GSVA and GSEABase packages, scoring 28 immune-related gene sets for each sample. The results were further analyzed to assess differences in immune cell infiltration between groups.

Molecular Docking Study

The structure of TP53 protein (PDB ID: 3D06) was downloaded from the Protein Data Bank (PDB) database. The Protein Preparation Wizard module in Schrödinger software was used for protein structure pretreatment, including hydrogenation, residue modification, removal of irrelevant ligands and water molecules, and energy minimization optimization under OPLS3e force field. Subsequently, the Binding Site Detection module was used to predict the active pocket of the protein, and the Receiver Grid Generation module was used to set the grid center at the predicted active pocket, with a box size of 20 Å × 20 Å × 20 Å.

The small molecule compound Hydroxysafflor Yellow A (PubChem CID: 6443665) was downloaded from the PubChem database and subjected to docking pretreatment using the LigPrep module under the OPLS3e force field, including ionization state generation, conformation search, and energy optimization. The docking calculation adopts the Ligand Docking module in Schrödinger, which performs flexible docking in Standard Precision (SP) and Extra Precision (XP) modes. Finally, the binding energy was calculated using the Molecular Mechanics Generalized Born Surface Area (MM-GBSA) method.

Molecular Dynamics Simulation

To evaluate the stability of HSYA within the TP53 binding pocket, a 100-ns molecular dynamics (MD) simulation of the HSYA-TP53 complex was carried out using the Desmond module of the Schrödinger software suite. The system uses the water model TIP3P, with the protein ligand complex solvent box set as a 1nm square, neutralized by ion addition, and energy minimized using the OPLS3 force field. Following a 1-ns equilibration, a 100-ns production run was conducted under NPT conditions at 300 K. The simulation analysis included root mean square deviation (RMSD), root mean square fluctuation (RMSF), ligand-protein contact mapping, and comprehensive evaluation of the binding profile.

Animal Preparation and Sepsis Model

Eight-week-old specific pathogen-free (SPF) C57BL/6 mice (20–22 g) were acclimatized for 24 h under controlled conditions (temperature, 22 ± 2 °C; humidity, 40%–70%). Sepsis was induced by CLP. Mice were anesthetized via intraperitoneal injection of sodium pentobarbital (30 mg/kg). After confirming the absence of a pain reflex, the animals were placed on a surgical board, disinfected with povidone-iodine, and subjected to a ~1 cm midline abdominal incision.

In the sham group, exploratory laparotomy was performed without ligation or puncture. In the sepsis (Sep), Ferrostatin-1 (Fer-1), Pifithrin-α, and HSYA groups, the cecum was exteriorized and ligated with sterile surgical suture (No. 4) at one-quarter of the distance from the cecal tip below the ileocecal valve. The distal cecum was punctured once with a sterile 22 G needle near the ligation site, passing through both sides, and ~0.2 mL of fecal content was extruded. The cecum was repositioned into the peritoneal cavity, and the incision was closed in layers with sterile suture (No. 2).

After surgery, mice were housed individually. Twelve hours post-CLP, mean arterial pressure (MAP) was measured via carotid artery cannulation and a ≥30% MAP reduction was considered a successful model. The Sep group of mice received no treatment after CLP. All drug solutions were prepared in dimethyl sulfoxide (DMSO) and saline, with a final DMSO concentration of 4% (v/v). One hour before model induction, the Fer-1 and Pifithrin-α groups received intraperitoneal injections of Fer-1 (1 mg/kg) or Pifithrin-α (5 mg/kg), respectively; the HSYA group received HSYA (10 mg/kg) via tail vein injection; the sham group mice received vehicle only.

Tissues were harvested 24 h after surgery. All procedures were approved by the Ethics Committee of the Army Medical University (approval number: AMUWEC20257048) and conducted in accordance with the Laboratory Animal Center of the Army Specialty Medical Center, Army Medical University (production license: SCXK [Yu] 2022–0011; use license: SYXK [Yu] 2022–0018).

Cell Culture and Reagents

Reagents

HSYA was purchased from Selleck (Houston, TX, USA). Pifithrin-α was obtained from Selleck (Houston, TX, USA). Malondialdehyde (MDA) and total glutathione/oxidized glutathione assay kits were supplied by Servicebio (Wuhan, China). Enzyme-linked immunosorbent assay (ELISA) kits for tumor necrosis factor-α (TNF-α), interleukin-6 (IL-6), and interleukin-1β (IL-1β) were purchased from Elabscience (Wuhan, China). Lipopolysaccharide (LPS) and type I collagenase were purchased from Sigma-Aldrich (St. Louis, MO, USA). Ferrostatin-1 was obtained from MedChemExpress (Monmouth Junction, NJ, USA). Antibodies against GPX4, xCT, COX2, and β-actin, as well as goat anti-rabbit primary and secondary antibodies, were purchased from Abcam (Cambridge, UK). The lipid peroxidation probe BODIPY 581/591 C11 was purchased from Thermo Fisher Scientific (Waltham, MA, USA). FerroOrange probe and Fe^{2+} assay kit were obtained from Dojindo (Kumamoto, Japan). Lipid hydroperoxide (LPO) assay kits were purchased from Jiancheng Bioengineering Institute (Nanjing, China). JC-1 mitochondrial membrane potential probe and reactive oxygen species (ROS) assay kit were purchased from Beyotime Biotechnology (Shanghai, China). Dulbecco's Modified Eagle Medium (DMEM) and fetal bovine serum (FBS) were purchased from HyClone (Logan, UT, USA).

IEC-6 Cell Culture

The IEC-6 cell line (American Type Culture Collection, ATCC, USA) was cultured in DMEM supplemented with 10% FBS in sterile culture dishes. Cells were maintained in a humidified incubator at 37 °C with 5% CO_2. When cell confluence reached 75%–80%, treatments were applied as follows: the Fer-1 group received 12 μM Ferrostatin-1 for 12 h; the HSYA group received 10 μM HSYA for 12 h; the Pifithrin-α group received 20 μM Pifithrin-α for 1 h. Following pretreatments, all experimental groups except the control were exposed to 10 μg/mL LPS for 12 h. The control (CTL) group was incubated with serum-free DMEM for 12 h.

Measurement of Malondialdehyde, Glutathione, and Iron Levels in Tissues

Levels of MDA, GSH, and iron in mouse lung and intestinal tissues were measured using specific assay kits. GSH levels were quantified with a total GSH/oxidized GSH (T-GSH/GSSG) assay kit, MDA levels were determined using an MDA assay kit, and ferrous iron (Fe^{2+}) concentrations were measured with a ferrous iron assay kit.

Quantification of Cytokines

Cytokine levels, including TNF-α, IL-1β, and IL-6, in cell culture supernatants and mouse serum were quantified using ELISA.

https://doi.org/10.2147/IDR.S528964

Histopathological Examination of Intestinal and Lung Tissues

Mice were euthanized by intraperitoneal injection of an overdose of sodium pentobarbital. Lung and ileal tissues were collected and fixed in 4% paraformaldehyde for 48–72 h. Tissues were then cut into 2–3 mm sections, dehydrated, cleared, paraffin-embedded, sectioned, stained with hematoxylin and eosin (H&E), and mounted. Histopathological changes were examined under a light microscope.

Transmission Electron Microscopy (TEM)

Following euthanasia by intraperitoneal injection of an overdose of sodium pentobarbital, a 10 cm segment of small intestine proximal to the stomach was excised and rinsed alternately with PBS and sodium citrate to remove fecal content. Both ends were ligated, and 2.5% glutaraldehyde was injected into the intestinal lumen. After 20 min, the intestine was cut into 1–2 mm segments and immersed in 2.5% glutaraldehyde for 30 min at room temperature, followed by transfer to sucrose solution at 4 °C for 2 h. Samples were post-fixed in osmium tetroxide for 2 h in the dark, dehydrated through a graded acetone series, and infiltrated with an acetone–resin mixture (1:1) for 1.5 h at room temperature. Resin embedding was performed at 37 °C for 24 h, followed by polymerization at 60 °C for 48 h. Ultrathin sections were stained with lead citrate and uranyl acetate, and ultrastructural changes were observed using a TEM (H-7500, Hitachi, Japan).

Western Blotting

Total protein was extracted from cells or tissues using RIPA lysis buffer supplemented with protease inhibitors. Protein concentrations were quantified with a BCA protein assay kit. Equal amounts of protein were resolved by SDS-PAGE and transferred to PVDF membranes. Membranes were blocked with 5% non-fat milk for 2 h at room temperature and incubated overnight at 4 °C with primary antibodies against GPX4, COX2, and xCT (1:1000 each) or β-actin (1:5000). After three washes with TBST, membranes were incubated with HRP-conjugated secondary antibodies at room temperature for 1 h. Protein bands were visualized using an Enhanced Chemiluminescence (ECL) detection system, and signal intensities were quantified with ImageJ software.

Detection of Cellular Lipid Peroxidation and ROS

Lipid peroxidation was evaluated using a fluorescent probe that shifts emission from red to green upon reaction with lipid peroxides. Following the indicated treatments for 24 h, cells were washed twice with PBS, incubated with the probe at 37 °C in 5% CO_2 for 30 min, washed again to remove excess probe, and analyzed by laser scanning confocal microscopy.

Intracellular ROS levels were measured using a ROS detection kit. Cells were stained with Hoechst 33258 to label nuclei, washed with PBS, and incubated with the ROS detection reagent at 37 °C in 5% CO_2 for 30 min. After a final wash, fluorescence signals were observed by laser scanning confocal microscopy.

Animal Survival

Sixteen mice per group were randomly assigned using a random number table Survival time and survival rate were recorded over a 72-h period starting 12 h after CLP surgery.

Statistical Analysis

All statistical analyses were performed using R software (version 4.0.2; https://www.r-project.org/). Continuous variables with normal distribution were compared between two groups using the independent Student's *t*-test, while non-normally distributed variables were analyzed using the Mann–Whitney *U*-test (Wilcoxon rank-sum test). Receiver operating characteristic (ROC) curves were plotted with the pROC package to evaluate the predictive performance of binary classification variables. All statistical tests were two-sided, and $P < 0.05$ was considered statistically significant.

Results

Bioinformatics Analysis Identified TP53 as a Key Ferroptosis-Related Gene in Sepsis

Analysis of the GSE28750, GSE57065, and GSE95233 datasets identified 708, 681, and 1,011 DEGs, respectively, when comparing sepsis samples with controls. The top 40 DEGs from each dataset were visualized in heatmaps (Figure 1A–C). A total of 638 FRGs were obtained from the FerrDb and GeneCards databases. Intersecting these FRGs with the DEGs from the three datasets yielded 15 commonly downregulated and 19 commonly upregulated genes (Figure 1D–E). An ANN model was constructed based on the 34 intersecting genes, and ROC curve analysis was performed to assess diagnostic performance. In both training and test sets of GSE28750, GSE57065, and GSE95233, the area under the receiver operating characteristic curve (AUC) reached 1.000 (Supplementary Figure 1A). The marked difference in AUC values between training and test sets indicated potential overfitting of the model. To further identify candidate genes of diagnostic significance, PPI network analysis was performed using the STRING database and Cytoscape software. Degree centrality analysis ranked *TP53* highest, highlighting its central position within the ferroptosis-related DEG network (Figure 1F). As a core hub, *TP53* displayed the most extensive interactions with other genes, suggesting that its modulation could affect multiple ferroptosis-associated pathways in sepsis. These findings indicate that *TP53* dysfunction may play a pivotal role in sepsis-related ferroptosis mechanisms. When focusing solely on *TP53*, ROC analysis of training and test sets from the three datasets yielded AUC values of 0.972 and 1.000 (GSE28750), 0.998 and 1.000 (GSE57065), and 1.000 and 0.944 (GSE95233), demonstrating consistent results and confirming the robustness of *TP53* as a potential biomarker (Supplementary Figure 1B).

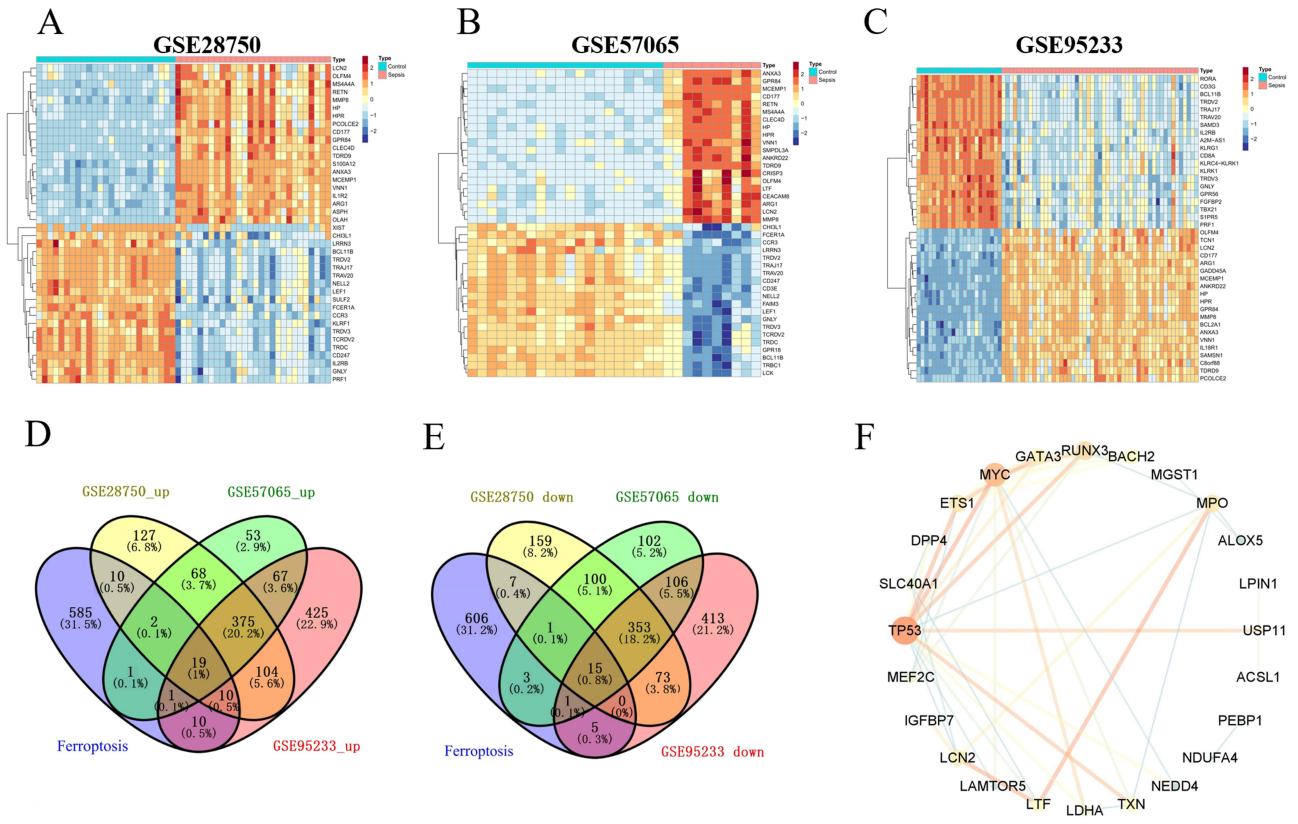

Figure 1 Identification and analysis of differentially expressed ferroptosis-related genes (FRGs) in sepsis. (**A**–**C**) Heatmaps showing the top 40 differentially expressed genes (DEGs) in sepsis versus control samples from the GSE28750, GSE57065, and GSE95233 datasets. (**D** and **E**) Venn diagrams illustrating the overlap between ferroptosis-related genes and DEGs in the three datasets, highlighting 15 commonly downregulated and 19 commonly upregulated genes. (**F**) Protein–protein interaction (PPI) network of the 34 intersecting FRGs, constructed using the STRING database and visualized in Cytoscape, with TP53 ranked as the top hub gene by degree centrality analysis.

https://doi.org/10.2147/IDR.S528964

TP53 is Expressed at Low Levels in Peripheral Blood Cells During Sepsis

To evaluate the cell-type-specific expression patterns of TP53 in sepsis, we analyzed the single-cell RNA-seq dataset GSE175453. Dimensionality reduction was performed using the top 20 principal components. Subsequent unsupervised clustering was conducted using the functions FindNeighbors and FindClusters with a resolution parameter of 1.0, which identified 26 distinct cell clusters (Figure 2A). Cell type annotation was performed by integrating canonical markers from the literature with automated referencing using the SingleR package. This analysis defined all major immune lineages: monocytes (clusters 0, 1, 2, 3, 4, 7, 10, 15, 22); $CD4^+$ T cells (clusters 6, 9); $CD8^+$ T cells (cluster 8); other T cells (clusters 14, 16); B cells (cluster 13); natural killer (NK) cells (cluster 5); innate lymphoid cells (ILCs; clusters 17, 21); dendritic cells (DCs; cluster 12); plasmacytoid DCs (pDCs; cluster 19); plasma cells (cluster 23); mast cells (cluster 25); platelets (clusters 11, 18); and a distinct cluster of cycling cells (cluster 24) (Figure 2B).

Expression analysis of the top 12 hub genes ranked by degree centrality revealed that *TP53* was detectable across all clusters. As a pivotal tumor suppressor, *TP53* is typically enriched in highly proliferative and genomically unstable cells, reflecting its short half-life and rapid turnover. In contrast, most peripheral blood cells, except hematopoietic stem cells, are terminally differentiated and require minimal *TP53*-mediated cell cycle regulation. Consistent with this, single-cell sequencing of peripheral blood from patients with sepsis showed uniformly low *TP53* expression across immune cell clusters (Figure 2C–E).

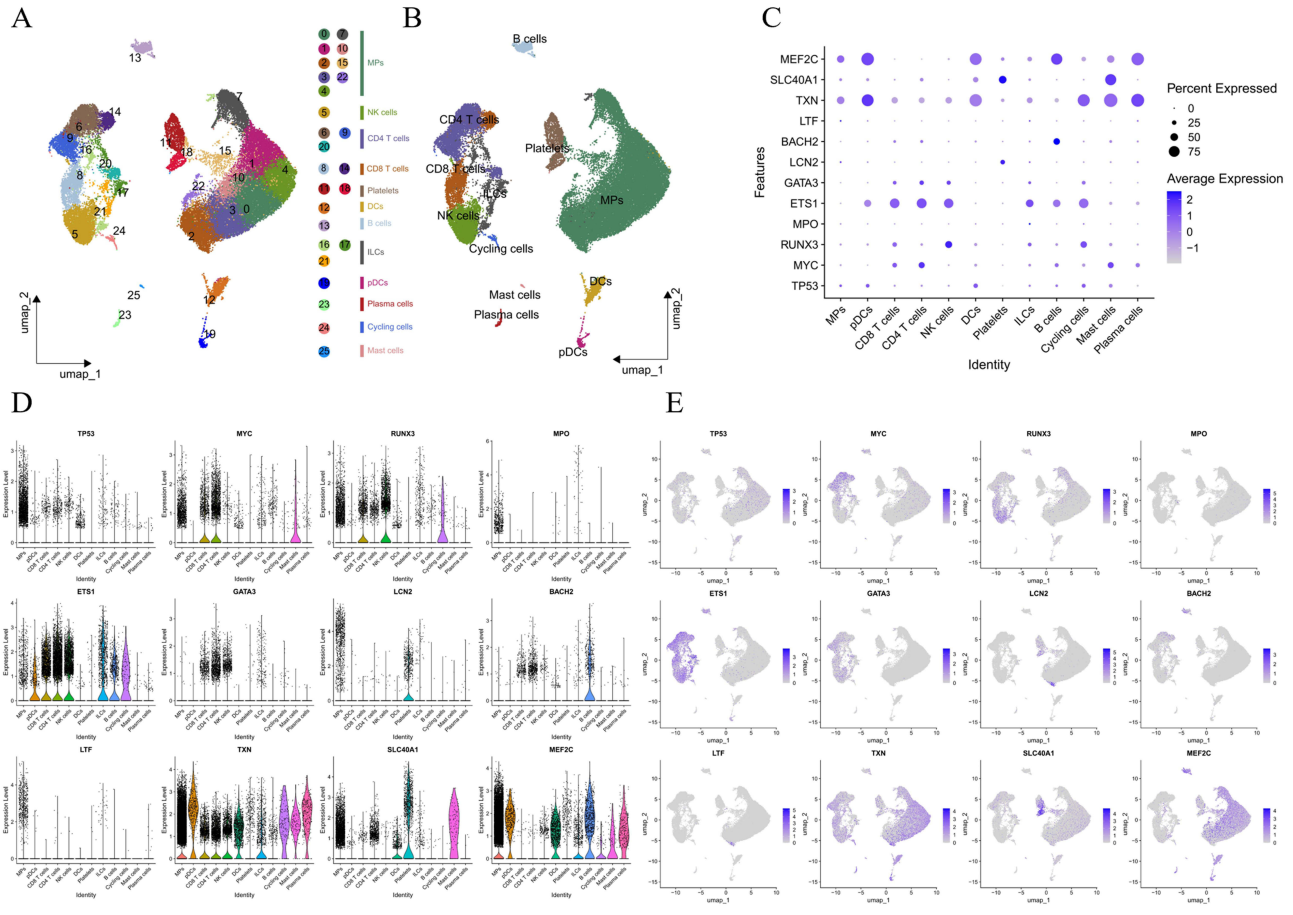

Figure 2 Single-cell RNA-seq analysis of immune cells in sepsis. (**A**) UMAP plot of 25 clusters identified from integrated single-cell datasets. (**B**) UMAP plot annotated with immune cell types assigned using the SingleR package. (**C–E**) Heatmap, violin plots, and bubble plots showing the expression profiles of TP53 and other hub genes across the 25 immune cell clusters.

Functional Prediction of TP53 Through KEGG, GO, and GSEA Analyses

Sepsis samples from the GSE57065 and GSE95233 datasets were subjected to in-depth single-gene analysis of *TP53*. Based on *TP53* expression levels, samples were divided into high- and low-expression groups, and DEGs were identified between the two groups (Figure 3A). Given the importance of *TP53* in sepsis and its status as a DEG between sepsis and control groups, further subdivision of sepsis samples into *TP53*-high and *TP53*-low subgroups was performed. KEGG and GO enrichment analyses were then conducted to determine whether *TP53* expression could serve as a functional marker and to characterize functional differences associated with its expression profile.

KEGG pathway analysis of the GSE57065 dataset revealed enrichment in immune-related diseases (eg, rheumatoid arthritis), infection-associated pathways (eg, herpes simplex virus, Epstein–Barr virus), and core immune signaling cascades, reflecting the interplay between immune responses, infection, and disease progression. In the GSE95233 dataset, enriched pathways included immune diseases (eg, asthma, type 1 diabetes), immune core processes (eg, antigen

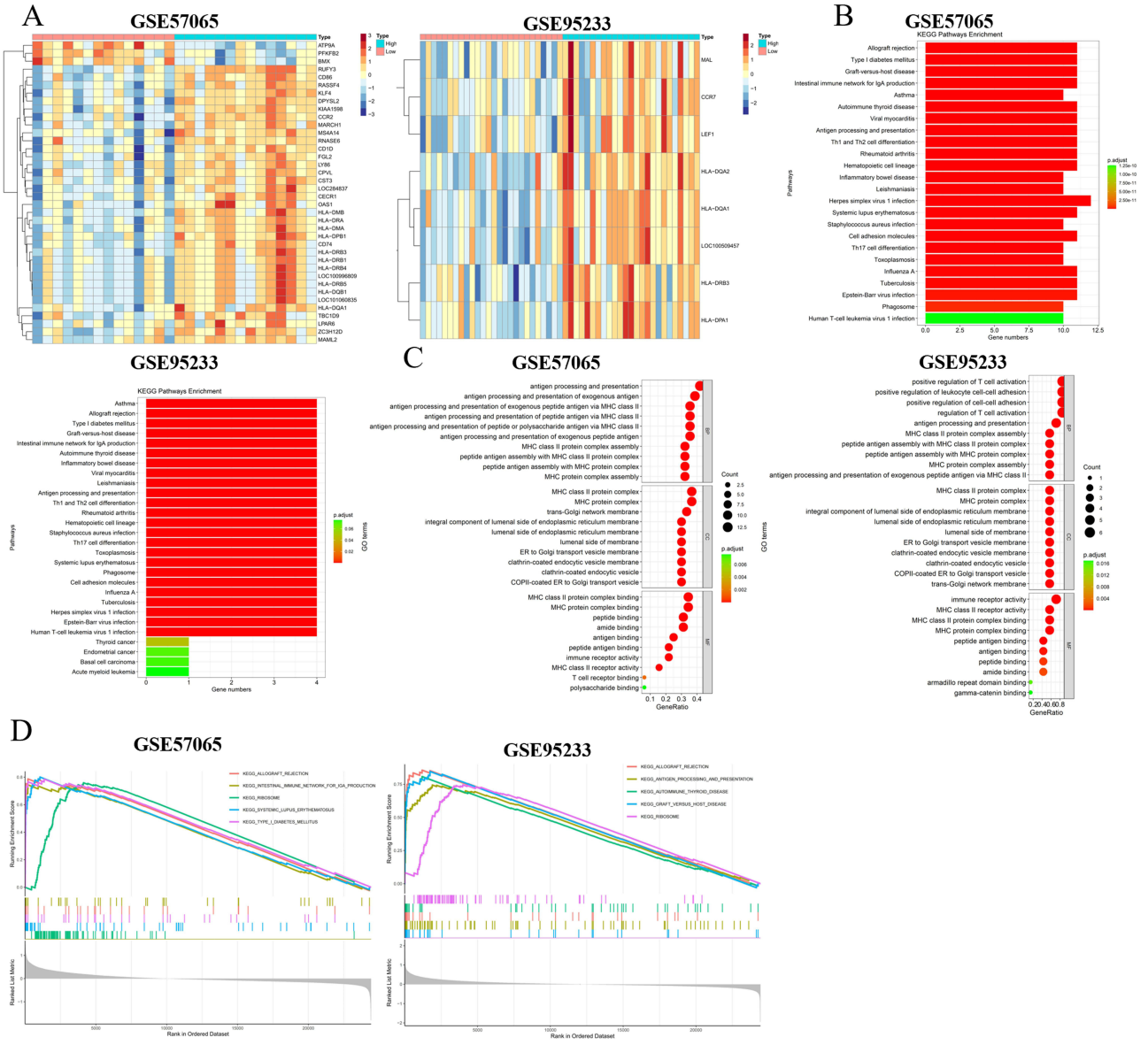

Figure 3 TP53 subgroup analysis and pathway enrichment. (**A**) Heatmaps showing differences in TP53 expression between high- and low-expression groups in the two datasets. (**B**) Bar plots presenting KEGG pathway enrichment of differentially expressed genes in the two datasets. (**C**) Bubble plots displaying GO enrichment analysis of differentially expressed genes in the two datasets. (**D**) Gene set enrichment analysis (GSEA) results for the two datasets.

https://doi.org/10.2147/IDR.S528964

processing and presentation, T helper cell differentiation), infection pathways (eg, Staphylococcus aureus, herpes simplex virus, Epstein–Barr virus), and cancer-associated pathways (eg, thyroid cancer) (Figure 3B).

GO analysis indicated that in the GSE57065 dataset, enriched terms spanned the immune response cascade from "basic antigen processing" to "dynamic regulatory activation", including MHC class II antigen processing, positive regulation of T-cell activation, and regulation of leukocyte and cell–cell adhesion, thereby outlining a complete sequence from antigen presentation to effector activation. In the GSE95233 dataset, enriched terms focused on the fundamental processes of MHC class II antigen processing and presentation, including MHC class II complex assembly, peptide antigen loading, and exogenous antigen presentation, highlighting core antigen-presentation pathways (Figure 3C). To mitigate potential bias from analyzing only DEGs, gene set enrichment analysis (GSEA) was performed on both datasets. GSE57065 exhibited enrichment in pathways such as allograft rejection, intestinal immune network for IgA production, ribosome, systemic lupus erythematosus, and type 1 diabetes. GSE95233 showed enrichment in allograft rejection, antigen processing and presentation, autoimmune thyroid disease, graft-versus-host disease, and ribosome pathways (Figure 3D). Collectively, these results highlight a close link between immune activation and remodeling of core cellular functions, providing an integrated pathway–gene–function framework for understanding immune regulatory mechanisms. The findings further emphasize the potential central role of *TP53* in the pathogenesis of sepsis.

Clustering of Ferroptosis-Related Subtypes in Sepsis and Associated Immune Characteristics

Consensus clustering based on the expression profiles of 34 ferroptosis-related differentially expressed genes was applied to sepsis samples from the GSE57065 and GSE95233 datasets. In both datasets, the optimal solution separated the samples into two distinct subtypes, designated Cluster 1 and Cluster 2 (Figure 4A). ssGSEA in the GSE57065 dataset demonstrated that Cluster 2 exhibited higher infiltration levels than Cluster 1 in most immune cell populations, including activated B cells, activated $CD8^+$ T cells, eosinophils, immature B cells, myeloid-derived suppressor cells (MDSCs), monocytes, natural killer T cells, neutrophils, conventional dendritic cells, effector memory $CD4^+$ T cells, central memory $CD4^+$ T cells, effector memory $CD8^+$ T cells, and central memory $CD8^+$ T cells. In the GSE95233 dataset, increased infiltration in Cluster 2 was observed for a subset of immune cell types, including activated B cells, activated $CD4^+$ T cells, $CD56^{bright}$ natural killer cells, immature dendritic cells, mast cells, T helper 17 (Th17) cells, T helper 2 (Th2) cells, and central memory $CD4^+$ T cells (Figure 4B).

Correlation analysis between *TP53* expression and immune-related genes across the GSE28750, GSE57065, and GSE95233 datasets revealed consistent co-expression patterns, suggesting that elevated *TP53* expression may enhance the transcription of multiple immune-related genes. These findings support the role of *TP53* as a potential central regulator of immune responses in sepsis, acting through the activation of diverse immune pathways.

Co-expression analysis in the GSE57065 dataset revealed predominantly positive correlations (indicated in blue) between *TP53* and members of the *HLA* gene cluster (eg, *HLA-DPA1, HLA-DPB1*), as well as *ICAM2* and *EEF2*, with varying correlation intensities. These patterns suggest potential interactions between *TP53*, immune adhesion molecules (*ICAM2*), and metabolism-related genes (*EEF2*), implying that *TP53* may influence immune cell function through an "immune–metabolism" crosstalk mechanism, thereby providing new insight into *TP53*-mediated immune dysregulation in sepsis. In the GSE28750 dataset, *TP53* showed variable positive correlations with *HLA* family genes (eg, *HLA-DRB3 /5, HLA-DMA/B), CD74*, and *CD4*. The strength of these associations suggests that *TP53* may engage in coordinated regulation with immune-related genes, potentially contributing to antigen presentation and immune cell activation through complex and context-specific mechanisms. Analysis of the GSE95233 dataset identified positive correlations between *TP53* and *MYC, IL27RA*, and *HLA-DQA1*, indicating a distinct interaction profile potentially involving the co-regulation of cytokine receptors (eg, *IL27RA*). These associations point to possible cross-regulatory roles of *TP53* in immune surveillance and inflammatory responses, offering clues for mechanistic studies in sepsis and other diseases (Figure 4C). The overall correlation patterns were consistent with immune cell infiltration results, showing a positive association between *TP53* expression and the infiltration levels of monocytes and other immune cell types (Figure 4D).

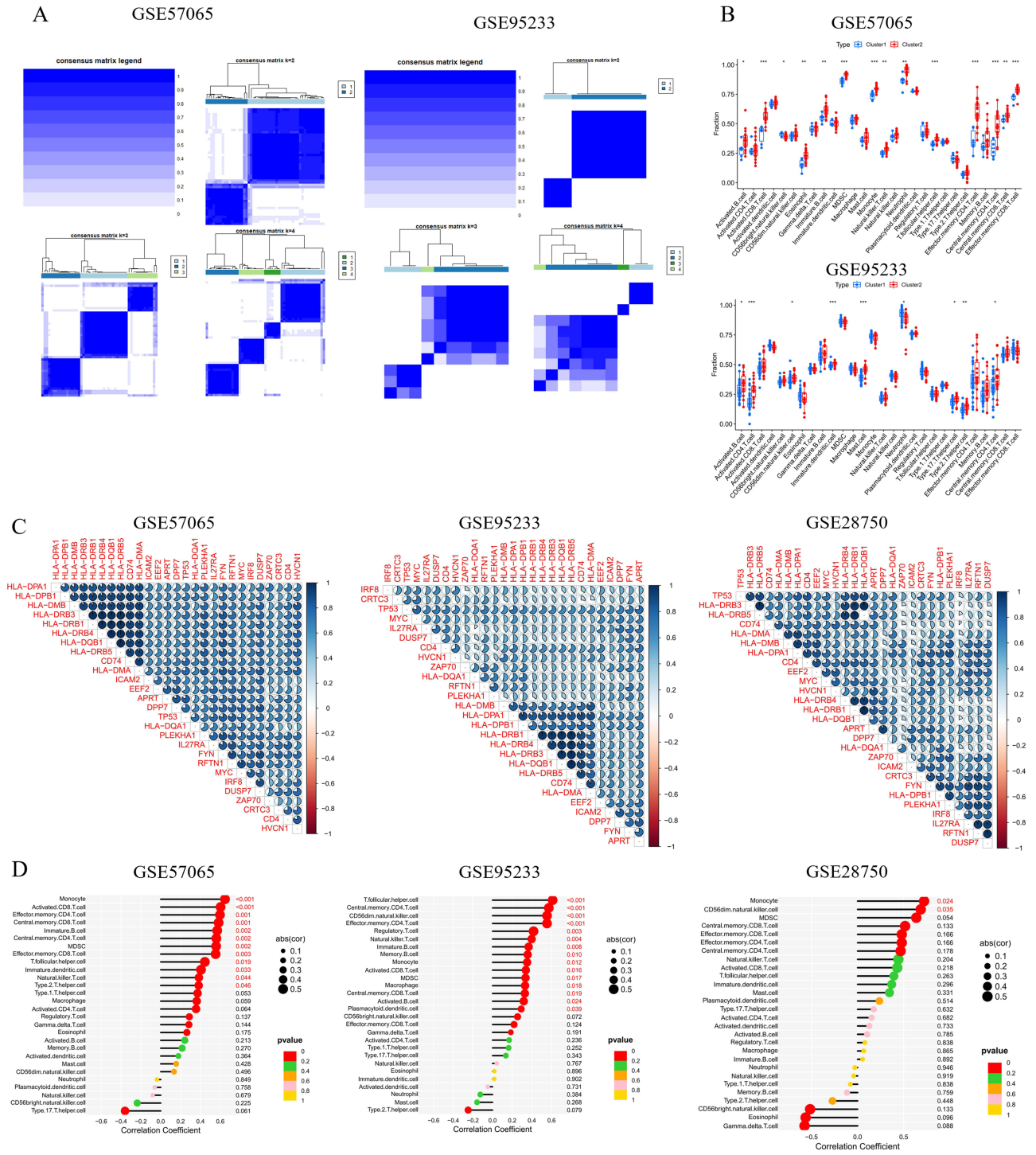

Figure 4 Comprehensive analysis of TP53 expression, immune response, and ferroptosis in sepsis. (**A**) Heatmaps showing consensus clustering results in the two datasets. (**B**) Box plots presenting differences in immune cell infiltration levels between clusters in each dataset. (**C**) Heatmaps illustrating co-expression patterns between immune-related genes and TP53 across the three datasets. (**D**) Lollipop charts displaying correlations between TP53 expression and immune cell infiltration in the datasets.

Ferroptosis Induction by CLP in Lung and Intestinal Tissues

The contribution of ferroptosis to sepsis-induced acute lung injury and intestinal barrier dysfunction was investigated using the ferroptosis inhibitor ferrostatin-1 (Fer-1) in a CLP-induced mouse model of sepsis. HE staining revealed marked pulmonary and intestinal injury in septic mice. Lung sections exhibited prominent neutrophil infiltration within

https://doi.org/10.2147/IDR.S528964

the alveolar walls, loss of alveolar architecture, and narrowing of alveolar spaces. Intestinal sections showed villus defects, goblet cell loss, shortened and edematous villi, goblet cell hyperplasia, and reduced lymphocyte numbers. Fer-1 pre-treatment markedly ameliorated these histopathological changes (Figure 5A and B). TEM demonstrated sparse, disorganized, and partially lost intestinal microvilli in septic mice, whereas Fer-1 restored villus integrity and orderly arrangement (Figure 5C). Fer-1 also significantly reduced systemic inflammation, with serum IL-1β, IL-6, and TNF-α levels decreasing by 43.87%, 57.08%, and 29.35%, respectively, compared with septic controls (Figure 5D). Additionally, 72 h survival analysis showed high early mortality in septic mice, with only two surviving beyond 72 hours (mean survival, 33.75 h). Fer-1 treatment significantly improved outcomes, with six mice surviving beyond 72 hours (mean survival, 47.5 h) (Figure 5E).

Biochemical assays demonstrated that Fer-1 reduced ferroptosis in both lung and intestinal tissues. In lung tissue, MDA and Fe^{2+} levels decreased by 26.19% and 38.68%, respectively, while GSH increased by 1.68-fold change. In intestinal tissue, MDA and Fe^{2+} levels decreased by 30.64% and 35.41%, with GSH increasing by 1.16-fold change (Figure 5F and G). Western blotting confirmed attenuation of ferroptotic activity by Fer-1, with increased GPX4 and xCT protein levels and reduced COX2 expression. In lung tissue, GPX4 and xCT increased by 48.65% and 30.16%, respectively, while COX2 decreased by 19.50%. In intestinal tissue, GPX4 and xCT increased by 62.73% and 33.54%, with COX2 reduced by 22.88%. TP53 protein expression in lung tissue decreased from 1.60 in septic mice to 1.28 in Fer-1–treated mice (20% reduction), and in intestinal tissue from 1.59 to 1.37 (13.84% reduction) (Figure 5H–P).

These findings indicate that ferroptosis is a key driver of sepsis-induced lung and intestinal injury. Pharmacological inhibition with Fer-1 not only alleviates tissue damage and systemic inflammation but also improves short-term survival in septic mice.

Inhibition of TP53 Alleviates Sepsis-Induced Ferroptosis

TP53, a key transcription factor, can promote ferroptosis by suppressing xCT expression, thereby reducing cystine uptake, impairing glutathione synthesis, and decreasing GPX4 activity. In this study, TP53 expression was markedly upregulated in both intestinal and lung tissues following sepsis and was attenuated by ferroptosis inhibition. To further investigate the role of TP53 in sepsis, the TP53-specific inhibitor Pifithrin-α was employed.

HE staining and TEM (Figure 6A–C) revealed that TP53 inhibition significantly ameliorated pathological damage in the lung and intestinal tissues of septic mice. Pifithrin-α markedly reduced systemic inflammation, as indicated by serum IL-1β, IL-6, and TNF-α levels decreasing by 42.19%, 59.97%, and 30.23%, respectively, compared with septic controls (Figure 6D). In 72-hour survival assays, septic mice displayed high early mortality, with only one animal surviving beyond 72 hours (mean survival, 28 h). Pifithrin-α treatment substantially improved survival, with 11 mice surviving beyond 72 hours (mean survival, 57 h) (Figure 6E).

Biochemical analyses demonstrated that Pifithrin-α markedly reduced ferroptosis in both lung and intestinal tissues. In lung tissue, MDA and Fe^{2+} levels decreased by 28.76% and 38.49%, respectively, while GSH increased by 1.48-fold change. In intestinal tissue, MDA and Fe^{2+} levels decreased by 32.67% and 33.68%, with GSH increasing by 1.73-fold change (Figure 6F and G). Western blot analysis further confirmed attenuation of ferroptotic activity by Pifithrin-α. In lung tissue, GPX4 and xCT protein levels increased by 1.17-fold change and 0.83-fold change, respectively, while COX2 decreased by 16.82%. In intestinal tissue, GPX4 and xCT increased by 69.51% and 0.98-fold change, while COX2 decreased by 20.17%. Notably, TP53 protein expression in lung tissue decreased from 1.55 in septic mice to 1.35 in the Pifithrin-α group (19.20% reduction), and in intestinal tissue from 1.69 to 1.27 (24.85% reduction) (Figure 6H–P).

These findings indicate that TP53 inhibition modulates ferroptosis-related markers, including GPX4 and xCT, and plays a critical role in sepsis-induced lung and intestinal injury. Targeting TP53 may represent a promising therapeutic strategy for sepsis.

LPS Induces Ferroptosis in IEC-6 Cells, withTP53 as a Key Target

Based on single-cell sequencing results showing low *TP53* expression in blood cells, in vitro experiments were conducted using IEC-6 cells to investigate *TP53* expression in tissue-derived cells.

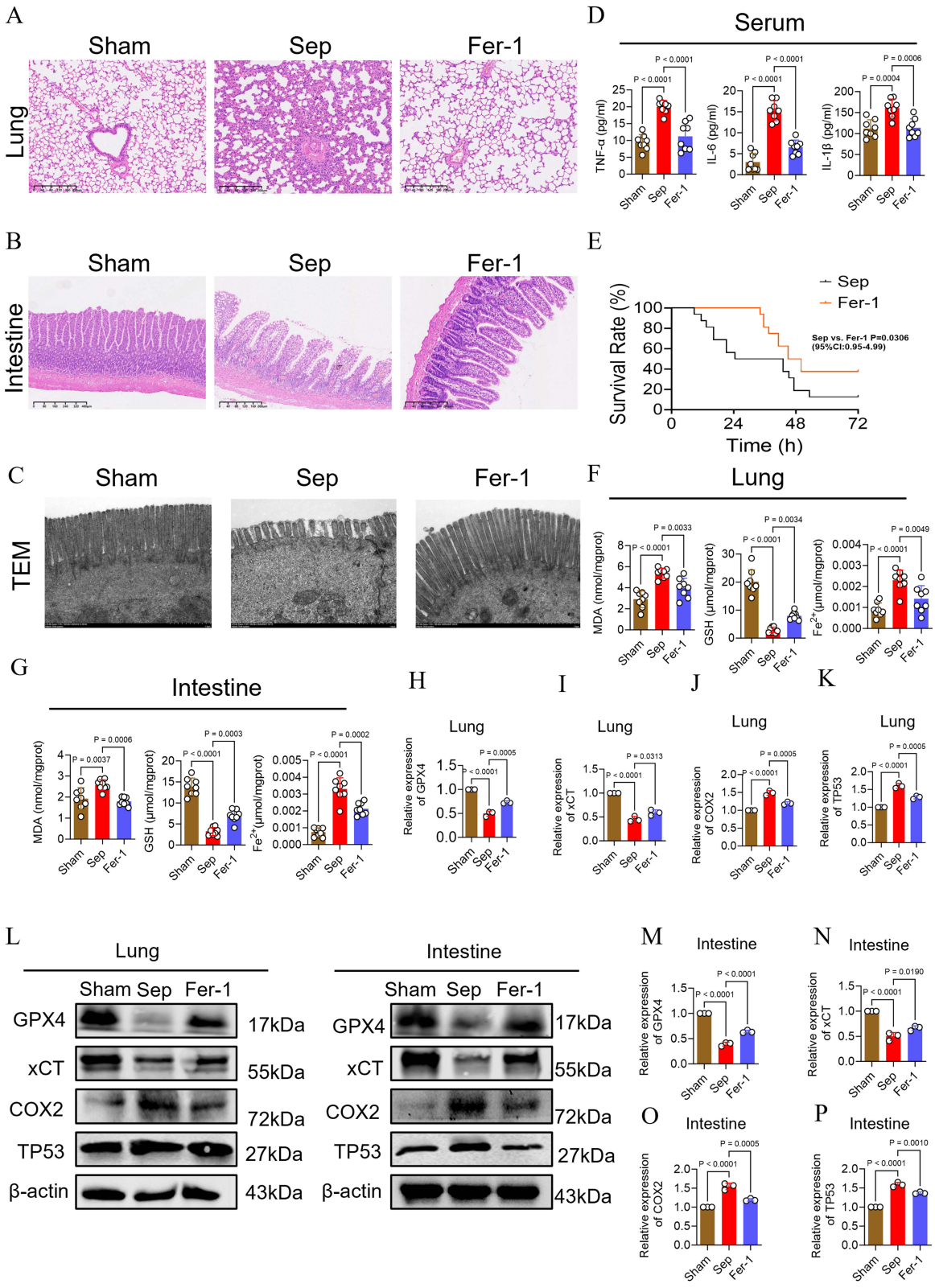

Figure 5 Ferroptosis induced by CLP in lung and intestinal tissues. (**A–C**) Representative HE-stained lung and intestinal sections, and representative intestinal electron microscopy images (HE: scale bar = 40 μm; TEM: scale bar =1 μm). (**D**) Serum TNF-α, IL-1β, and IL-6 levels (n=8) indicate the severity of inflammation. (**E**) Effects of Fer-1 on survival in septic mice (n=16 per group). (**F**) MDA, GSH, and Fe^{2+} levels in lung tissue (n=8), assessing lipid peroxidation, ferroptosis markers, and antioxidant capacity. (**G**) MDA, GSH, and Fe^{2+} levels in intestinal tissue (n=8), assessing the same parameters as in lung tissue. (**H–P**) Western blot analysis of GPX4, xCT, and COX2 protein expression in lung and intestinal tissues (n=3).

https://doi.org/10.2147/IDR.S528964

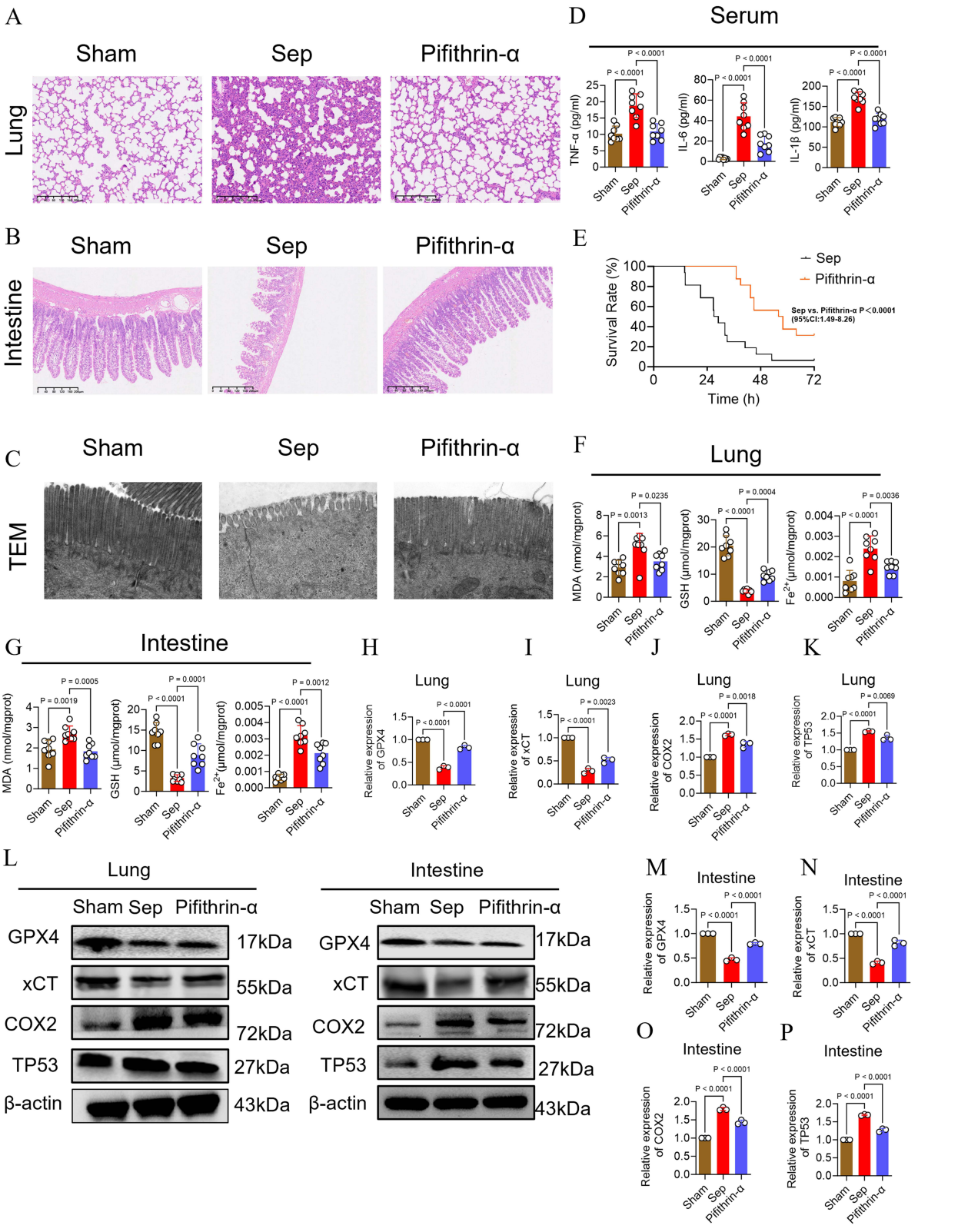

Figure 6 Targeting TP53 attenuates ferroptosis in sepsis. (**A**–**C**) Representative hematoxylin–eosin (HE) staining of lung and intestinal tissues and transmission electron microscopy (TEM) images of intestinal villi (HE: scale bar = 40 μm; TEM: scale bar=1 μm). (**D**) Serum concentrations of TNF-α, IL-1β, and IL-6 (n=8). (**E**) Effects of Pifithrin-α on survival in septic mice (n=16 per group). (**F**) Measurements of MDA, GSH, and Fe^{2+} in lung tissue (n=8) to assess lipid peroxidation, ferroptosis, and antioxidant capacity. (**G**) Measurements of MDA, GSH, and Fe^{2+} in intestinal tissue (n=8) using the same parameters as in panel C. (**H**–**P**) Western blot analysis of GPX4, xCT, and COX2 protein expression in lung and intestinal tissues (n=3).

https://doi.org/10.2147/IDR.S528964

To evaluate ferroptosis in IEC-6 cells after LPS stimulation, cells were pretreated with the ferroptosis inhibitor Fer-1 or the TP53 inhibitor Pifithrin-α prior to LPS exposure. Relative to untreated controls, LPS treatment caused a marked reduction in cell viability, accompanied by significant increases in the fluorescence intensity of lipid peroxides (LPO) and ROS. The fluorescence signal of Fe^{2+}, a key inducer of ferroptosis, was also markedly elevated, indicating disruption of intracellular iron homeostasis. Intracellular GSH content, a critical antioxidant, was substantially reduced, suggesting impaired free radical scavenging capacity, whereas MDA, a terminal lipid peroxidation product, was significantly elevated, confirming oxidative damage. Fer-1 or Pifithrin-α pretreatment markedly improved cellular status compared with the LPS group. Cell viability increased by 65.9% and 36.32%, respectively. LPO fluorescence intensity decreased by 69.63% and 88.13%, while ROS fluorescence decreased by 42.18% and 50.73%. Fe^{2+} fluorescence intensity was reduced by 60.01% and 55.06%, suggesting restoration of iron homeostasis. In addition, GSH content and MDA levels returned toward baseline, with GSH increasing by 2.39-fold change and 2.66-fold change, and MDA decreasing by 75.25% and 58.6%, respectively, relative to the LPS group (Figure 7A–F). These results indicate that Fer-1 and Pifithrin-α effectively restore antioxidant defenses, reduce lipid peroxidation, and protect IEC-6 cells from LPS-induced injury.

TEM showed mitochondrial swelling and a marked reduction in cristae after LPS exposure. Fer-1 and Pifithrin-α alleviated mitochondrial swelling and partially restored cristae density, with overall morphology approaching normal (Figure 7G). Western blot analysis further confirmed attenuation of ferroptotic activity by Fer-1 and Pifithrin-α (Figure 7H and I).

HSYA Mitigates Sepsis-Induced Ferroptosis

Molecular docking using the Glide program was performed to predict the binding mode of HSYA to TP53. The calculation results show that the score is −5.329 kcal/mol in SP mode, −7.438 kcal/mol in XP mode, and the binding energy of MM-GBSA is −33.99 kcal/mol, indicating that HSYA has good binding ability with TP53. Specifically, HSYA forms several conventional hydrogen bonds with the ASN A:131, THR A:102, and TYR A:126 residues of the TP53 protein, which serve as the key forces maintaining the stable binding between the two molecules. Meanwhile, the carbon-hydrogen bond formed with PRO A:128, though relatively weak, can enhance binding stability. Notably, the docking results indicated the presence of an unfavorable donor-donor interaction between the LEU A:111 residue of TP53 and HSYA, suggesting that this site may be a "weak region" in the binding; however, the overall binding is still dominated by other strong interactions. In addition, the pi-alkyl interaction (a hydrophobic interaction between aromatic rings and alkyl chains) formed between HSYA and the ARG A:110 residue further consolidates the binding stability between the ligand and the receptor (Figure 8A and B; Supplementary Figure 2A). Subsequent 100-ns MD simulations using the Desmond module further assessed the stability, structural dynamics, and molecular flexibility of the HSYA–TP53 complex. Molecular dynamics simulations indicate that the RMSD value fluctuates significantly within the first 40 ns of the simulation. After 40 ns, it stabilizes and remains within 0.1 nm.The RMSF reflects the flexibility changes of each amino acid residue in TP53. The RMSF value is relatively low between residues 100–110 and 130–150, suggesting that this region may be a binding pocket.demonstrating stable binding (Supplementary Figure 2B).

To investigate the therapeutic effects of HSYA in sepsis, IEC-6 cells were treated with HSYA and assessed for ferroptosis-related parameters. Compared with the LPS group, HSYA increased cell viability by 97.93% and markedly reduced intracellular fluorescence intensities of LPO, ROS, and Fe^{2+} by 71.88%, 68.73%, and 60.56%, respectively (Figure 8C–H). HSYA also restored antioxidant capacity, with MDA levels decreasing by 70.33% and GSH levels increasing by 3.25-fold change relative to the LPS group (Figure 8I and J).

TEM revealed that HSYA mitigated mitochondrial swelling and restored cristae density, with overall morphology approaching normal compared with the LPS group (Figure 8D). Western blot analysis further confirmed attenuation of ferroptotic activity by Fer-1 and Pifithrin-α (Figure 8K and L). These findings indicate that HSYA effectively alleviates LPS-induced ferroptosis and mitochondrial damage in IEC-6 cells.

HSYA Attenuates Sepsis-Induced Ferroptosis by Inhibiting TP53

Based on the molecular docking and cell-based findings, the role of HSYA in modulating ferroptosis during sepsis was further validated in vivo. CLP mice received HSYA treatment, and the effects on TP53 expression and ferroptosis-related

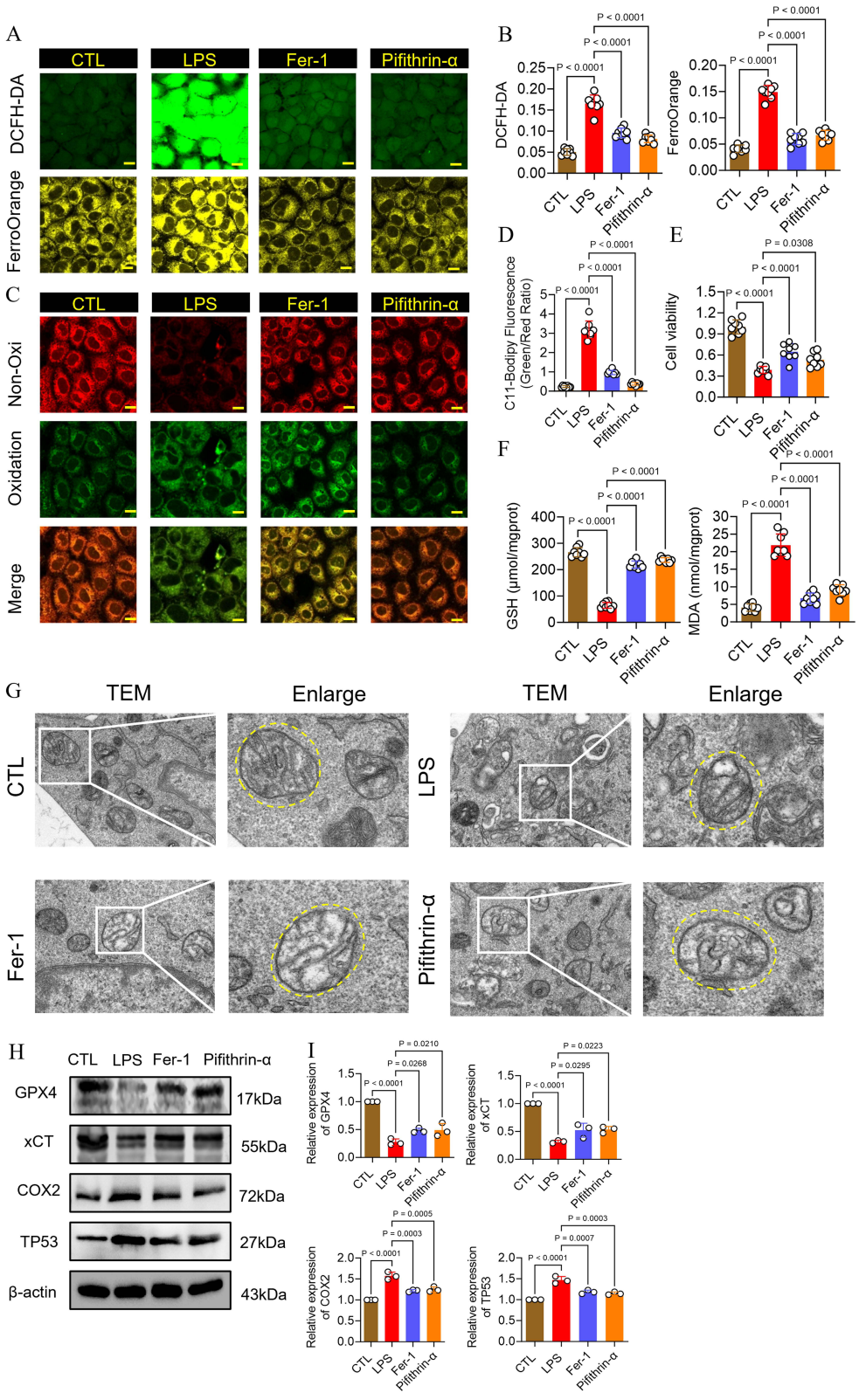

Figure 7 LPS induces ferroptosis in IEC-6 cells. (**A**) Representative fluorescence images showing the effects of Fer-1 and Pifithrin-α on intracellular Fe^{2+} and ROS levels in LPS-treated IEC-6 cells, detected using FerroOrange and DCFH-DA probes (scale bar = 50 μm). (**B**) Quantification of Fe^{2+} and ROS levels (n = 8). (**C**) Representative fluorescence images showing the effects of Fer-1 and Pifithrin-α on lipid ROS levels in LPS-treated IEC-6 cells, detected using the BODIPY™ 581/591 C11 probe (scale bar = 50 μm). (**D**) Quantification of LPO content (n = 8). (**E**) Effects of Fer-1 and Pifithrin-α on IEC-6 cell viability after LPS treatment, assessed using the CCK-8 assay (n = 8). (**F**) Intracellular GSH and MDA levels (n = 8). (**G**) Transmission electron microscopy images showing mitochondrial morphology in IEC-6 cells after LPS treatment, with or without Fer-1 or Pifithrin-α pretreatment (The structures labeled by yellow dotted circles in the figure are mitochondria). (**H** and **I**) Western blot analysis of GPX4, xCT, and COX2 protein expression in IEC-6 cells (n = 3). a: Sepsis/LPS group vs CTL group ($p < 0.05$); b: HSYA group vs Sepsis/LPS group ($p < 0.05$).

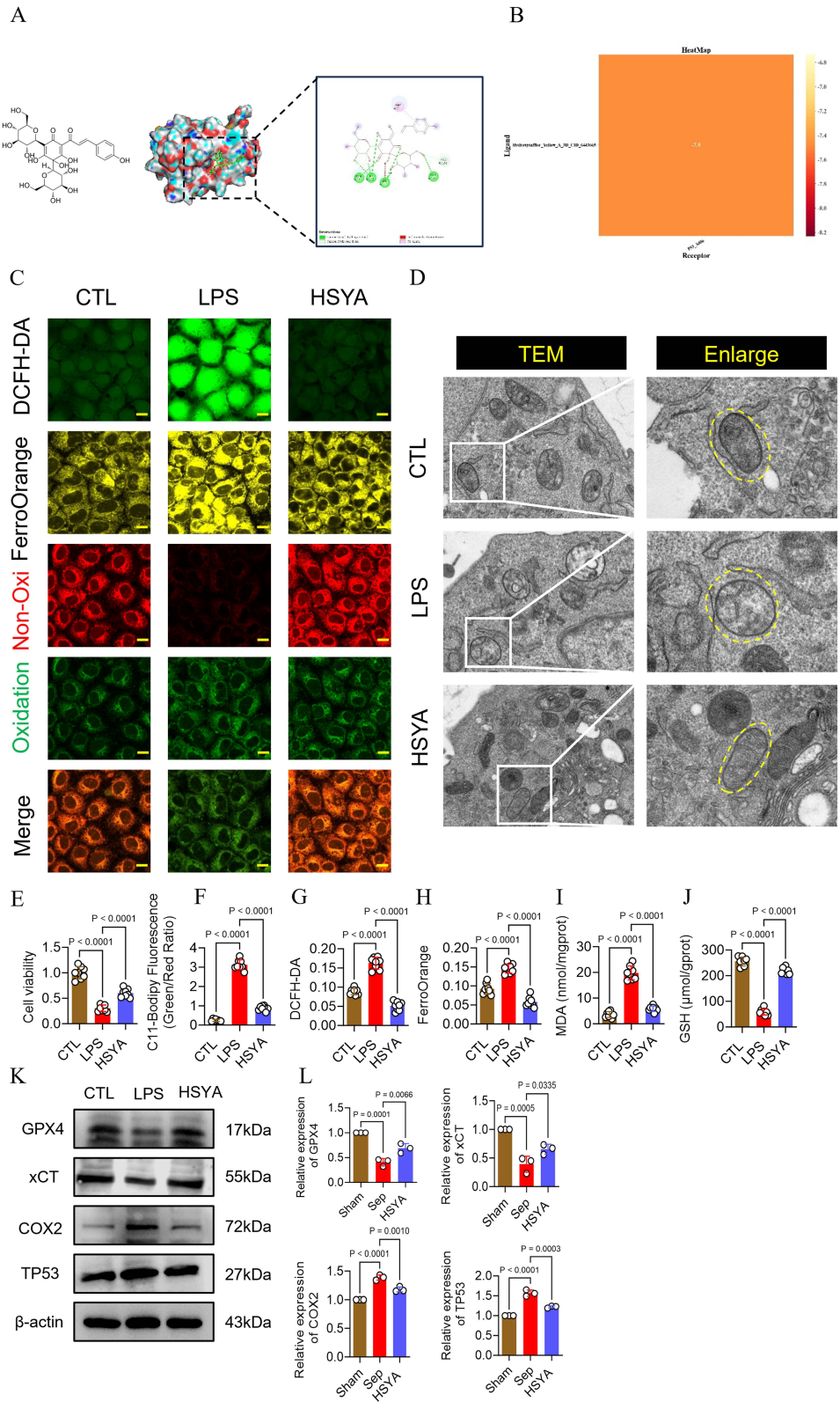

Figure 8 Molecular docking of HSYA with TP53 and in vitro effects on IEC-6 cells. (**A**) Predicted binding site and mode of HSYA on TP53. (**B**) Molecular docking simulation results for the HSYA–TP53 complex. (**C**) Representative fluorescence images showing the effects of HSYA on ROS, Fe^{2+}, and LPO levels in LPS-treated IEC-6 cells, detected using DCFH-DA, FerroOrange, and BODIPY™ 581/591 C11 probes (scale bar=50μm). (**D**) Transmission electron microscopy images showing mitochondrial morphology after HSYA treatment (The structures labeled by yellow dotted circles in the figure are mitochondria). (**E**) Cell viability after HSYA treatment (n=8). (**F**) LPO levels (n=8). (**G**) ROS levels (n=8). (**H**) Fe^{2+} levels (n=8). (**I**) MDA levels (n=8). (**J**) GSH levels (n=8). (**K** and **L**) Western blot analysis of GPX4, xCT, and COX2 protein expression in IEC-6 cells (n =3).

https://doi.org/10.2147/IDR.S528964

pathways were assessed. Histopathological examination of lung and intestinal tissues revealed that HSYA markedly ameliorated CLP-induced injury and restored normal architecture. Compared with the sepsis group, HSYA treatment substantially reduced neutrophil infiltration in alveolar spaces, decreased alveolar rupture, and alleviated alveolar wall edema and thickening. In the intestine, HSYA mitigated villus damage, shortening, and edema (Figure 9A and B). TEM revealed that HSYA markedly ameliorated pathological alterations in the intestinal tissues of septic mice (Figure 9C).

HSYA also attenuated the systemic inflammatory response. Serum IL-1β, IL-6, and TNF-α levels decreased by 35.94%, 51.59%, and 41.02%, respectively, relative to the sepsis group (Figure 9D). Ferroptosis-associated biochemical assays demonstrated significant reductions in MDA and Fe^{2+} levels, accompanied by increased GSH content, in both lung and intestinal tissues. In lung tissue, MDA and Fe^{2+} decreased by 51.93% and 60.32%, while GSH increased by 3.48-fold change. In intestinal tissue, MDA and Fe^{2+} decreased by 36.92% and 49.25%, and GSH increased by 45.22% (Figure 9E and F). Western blot analysis confirmed that HSYA modulated ferroptosis-related protein expression. In lung tissue, *GPX4* and *xCT* increased by 39.45% and 29.45%, respectively, while COX2 decreased by 12.94%. In intestinal tissue, *GPX4* and *xCT* increased by 74.71% and 60.79%, while COX2 decreased by 13.61%. Notably, TP53 protein expression in lung tissue decreased from 1.67 in the sepsis group to 1.54 in the HSYA group (7.78% reduction), and in intestinal tissue from 1.67 to 1.45 (13.17% reduction) (Figure 9G–O). Collectively, these findings demonstrate that HSYA mitigates sepsis-induced lung and intestinal injury, likely through inhibition of TP53-mediated ferroptosis, underscoring its therapeutic potential in sepsis-associated organ damage.

Discussion

Sepsis is a systemic inflammatory response syndrome caused by infection and is frequently observed in patients with severe trauma or infectious diseases. Sepsis and septic shock remain major global healthcare challenges, affecting millions of individuals each year and causing mortality in approximately one-third to one-sixth of cases.[34] Overactivation of inflammatory mediators disrupts immune regulation, creating a self-perpetuating and destructive positive feedback loop that triggers cytokine storms, ultimately leading to multi-organ injury involving the intestine, lungs, kidneys, and other organs, and resulting in death.[35–37] Current clinical management is primarily restricted to non-specific supportive interventions aimed at preserving organ homeostasis and limiting infection spread. Although early goal-directed therapy has yielded certain benefits in recent years, sepsis-related mortality remains unacceptably high.[38,39] As the intestine and lungs are primary targets in the pathogenesis of sepsis-induced multi-organ dysfunction, developing novel therapeutic strategies to address injury and functional impairment in these organs remains a critical priority in sepsis research.

Multi-organ dysfunction is a principal cause of mortality in sepsis, yet its underlying pathogenesis remains incompletely understood, and effective interventions are lacking. Patients remain at a substantially increased risk of treatment failure for weeks to months following disease onset, underscoring the importance of organ protection and functional support during this critical period.[40]

Ferroptosis, an iron-dependent form of regulated cell death distinct from apoptosis, is characterized by disrupted iron metabolism and excessive lipid peroxide accumulation. Accumulating evidence implicates ferroptosis as a key driver of sepsis pathology.[19,41] Targeting ferroptosis-related molecules has shown therapeutic potential. Bian et al demonstrated that inhibition of GPR116 mitigated sepsis-induced liver injury by modulating the Xc^- system/GSH/GPX4 pathway, thereby reducing ferroptosis, improving liver function, and enhancing survival in septic mice.[42] Li et al identified irisin as a critical regulator in sepsis-associated encephalopathy, where activation of the Nrf2/GPX4 axis attenuated ferroptosis, improved cognitive performance, alleviated neurological deficits, and restored the inflammatory microenvironment.[43] Similarly, Cui et al reported that Yiqi Fumai injection (YQFM) targeted the xCT/GPX4 axis to suppress ferroptosis in sepsis-induced cardiomyopathy, reducing myocardial injury and improving survival.[44]

Ferroptosis has emerged as a beneficial process in the context of sepsis, suggesting that ferroptosis-related genes may serve as potential therapeutic targets. Bioinformatic analysis of three sepsis datasets identified 34 ferroptosis-associated differentially expressed genes, among which PPI network analysis highlighted *TP53* as the most central node, underscoring its pivotal role in sepsis-associated ferroptosis. ROC analysis further confirmed the robustness and translational potential of *TP53* as a diagnostic marker. Single-cell transcriptomic profiling of peripheral blood from septic patients

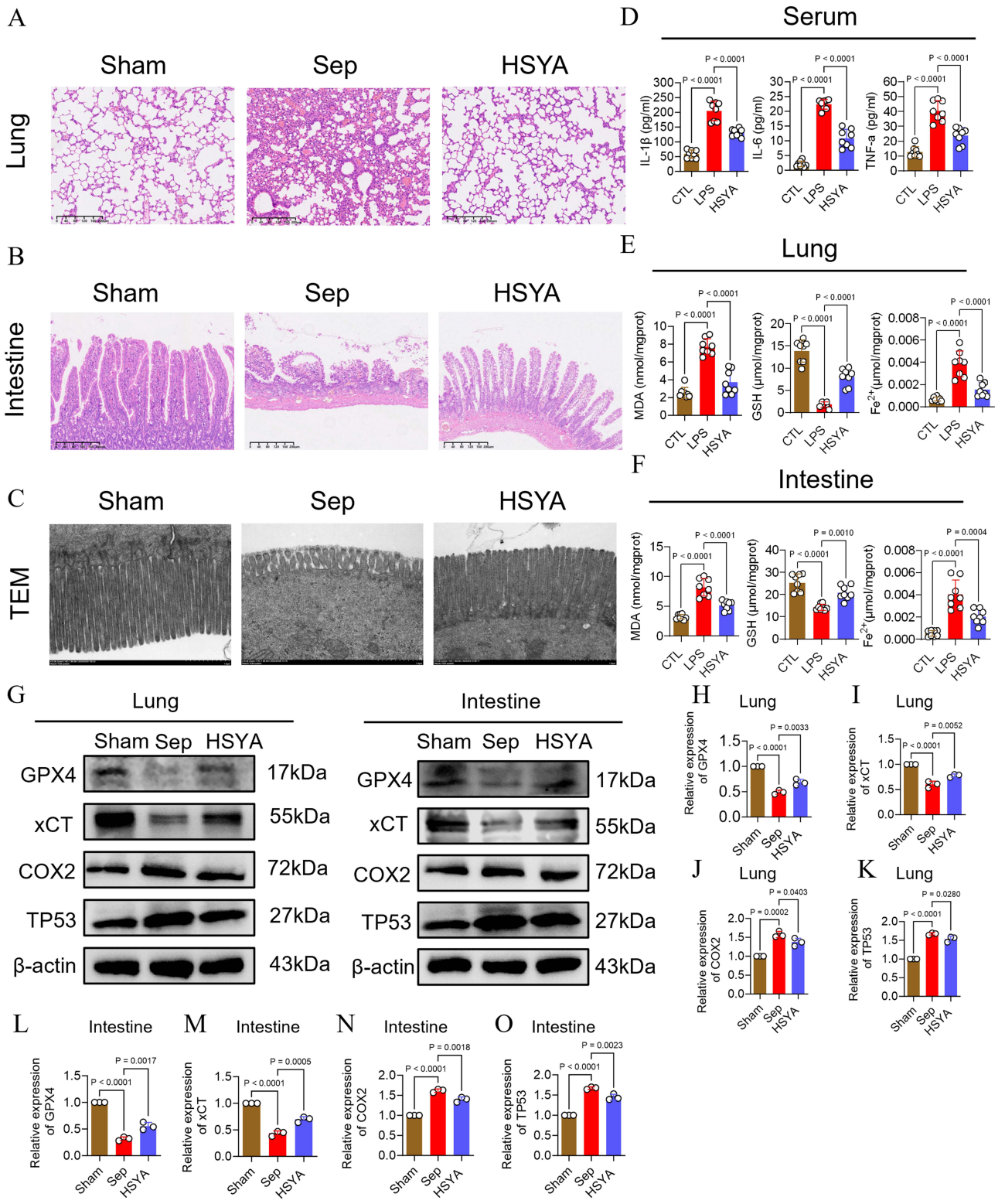

Figure 9 HSYA interacts with TP53 and alleviates sepsis-induced injury. (**A**–**C**) Representative hematoxylin–eosin (HE) staining of lung and intestinal tissues and transmission electron microscopy (TEM) images of intestinal villi (HE: scale bar = 40μm; TEM: scale bar =1μm). (**D**) Serum TNF-α, IL-1β, and IL-6 levels (n=8). (**E**) MDA, GSH, and Fe^{2+} levels in lung tissue (n=8), assessing lipid peroxidation, ferroptosis activity, and antioxidant capacity. (**F**) MDA, GSH, and Fe^{2+} levels in intestinal tissue (n=8), evaluated using the same parameters as in panel C. (**G**–**O**) Western blot analysis of GPX4, xCT, and COX2 protein expression in lung and intestinal tissues (n =3).

https://doi.org/10.2147/IDR.S528964

demonstrated uniformly low *TP53* expression across all identified cell clusters, consistent with prior reports that *TP53* in normal blood cells has a short half-life, unstable metabolism, and is maintained at low concentrations. Despite this, even low-level *TP53* expression was sufficient to activate downstream signaling pathways.[45] *TP53* is a master regulator of metabolic homeostasis, controlling processes such as glucose and lipid metabolism. It generally suppresses de novo lipogenesis and other anabolic pathways while promoting oxidative phosphorylation and catabolic metabolism. However, *TP53* exerts bidirectional effects, reflecting functional complexity that must be interpreted in disease-specific contexts.[46,47] The regulatory role of *TP53* in ROS homeostasis is particularly noteworthy. Under conditions of low ROS, caused by mild, transient, and reversible stress, *TP53* activates antioxidant pathways to lower ROS levels and protect cells. In contrast, when ROS levels become excessive due to severe, prolonged, and irreversible stress, *TP53* promotes further ROS accumulation, triggering cell death to protect surrounding tissues. As a central stress-response mediator, p53 preserves cellular homeostasis through such bidirectional regulation. Its activity requires precise balance: insufficient activation may fail to prevent injury, whereas excessive activation can induce unnecessary cell death, yielding both protective and harmful outcomes. This finely tuned and dynamic regulation underscores the essential role of p53 in cellular stress adaptation.[48–50]

In our in vivo experiments, attention was focused on lung and intestinal tissues, both of which are highly susceptible to injury and display characteristic pathological alterations during sepsis. The intestine, one of the earliest organs affected, plays a pivotal role in disease progression. Disruption of its barrier function facilitates bacterial and endotoxin translocation, thereby amplifying the systemic inflammatory response.[51] The lungs are similarly vulnerable, with inflammation and oxidative stress acting as key drivers of sepsis-induced acute lung injury.[52] During sepsis, reduced intestinal mucosal perfusion, diminished number and function of lamina propria plasma cells, and decreased secretory IgA (sIgA) secretion increase bacterial adhesion to epithelial cells and promote bacterial/endotoxin translocation. Intestinal hypoperfusion further leads to endothelial damage and barrier breakdown, intensifying systemic immune–inflammatory responses and contributing to secondary injury of the lungs and other organs. Lung injury, in turn, impairs oxygen delivery, exacerbating intestinal damage. This bidirectional interplay accelerates sepsis progression.[53–55] Pifithrin-α, a *TP53* inhibitor, has been widely used in both in vivo and in vitro studies.[56,57] Using the CLP model, we examined the contribution of ferroptosis to sepsis-induced lung and intestinal injury. In line with previous studies, tissues from CLP-induced septic mice exhibited hallmark ferroptotic features, including elevated MDA levels, decreased GSH content, and Fe^{2+} accumulation. Upregulation of *TP53* significantly mitigated tissue injury by suppressing lipid peroxidation and iron overload.[58,59] To further elucidate the link between *TP53* activity and ferroptosis in sepsis, we administered Pifithrin-α, which similarly alleviated lung and intestinal injury, consistent with earlier findings.[60–62] Mechanistically, the cystine/glutamate antiporter SLC7A11 (xCT) mediates cystine uptake for glutathione biosynthesis and antioxidant defense, whereas *TP53* downregulates xCT expression, thereby modulating ferroptosis and attenuating organ injury.[63,64] The role of *TP53* varies across different diseases and even between disease stages, underscoring the complexity and context-dependent nature of its functions in pathophysiology.

Few clinical trials have demonstrated the efficacy of iron chelation therapies in sepsis. XBJ, a traditional Chinese medicine injection, has been used clinically in China since its approval in 2004 and has shown therapeutic benefits in sepsis management. However, as a multi-component herbal formulation, XBJ exhibits complex pharmacological, distribution, and metabolic characteristics that are difficult to precisely define.[65] To address this, the present study focused on HSYA, a principal active constituent of XBJ. HSYA is a clinically applied, safe, low–molecular–weight natural compound.[66] Molecular docking and molecular dynamics simulations confirmed that HSYA binds stably to *TP53*, consistent with previous evidence indicating that HSYA suppresses TP53 signaling and oxidative stress.[67] Based on these findings, in vitro and in vivo experiments were conducted to elucidate the mechanism of HSYA in sepsis. HSYA significantly enhanced the viability of IEC-6 cells under septic conditions, reduced intracellular LPO, ROS, and Fe^{2+} levels, restored MDA and GSH balance, improved mitochondrial morphology, and attenuated ferroptosis. In septic mice, HSYA lowered serum levels of IL-1β, IL-6, and TNF-α. Consistent with earlier studies,[68] HSYA suppressed the release of inflammatory mediators and alleviated sepsis-associated ferroptosis, conferring substantial protective effects on both the intestine and lungs.

Although current research has partially elucidated how *TP53* mitigates sepsis-induced intestinal and pulmonary injury through ferroptosis regulation, important limitations remain. The role of *TP53* in sepsis is highly complex, with its regulation of ferroptosis potentially influenced by diverse signaling pathways and microenvironmental factors that remain incompletely defined. Moreover, the beneficial effects of *TP53*-mediated ferroptosis regulation observed in animal and cell models face considerable barriers to clinical translation. Future research should delineate the interactions between *TP53* and other signaling pathways to clarify the molecular basis of its ferroptosis regulation; undertake additional preclinical and clinical studies to evaluate the safety and efficacy of targeted interventions; employ gene-editing technologies to investigate *TP53* function more precisely; and develop novel compounds or biologics for targeted ferroptosis modulation, potentially in combination regimens, to enhance therapeutic outcomes in sepsis.

In conclusion, the study identified *TP53* as a pivotal therapeutic target in sepsis. Inhibition of *TP53* markedly ameliorated lung and intestinal injury in septic models. During disease progression, injury to these organs disrupts systemic immune homeostasis, a disturbance that can exacerbate multi-organ failure and increase mortality risk. Modulating *TP53*-mediated ferroptosis holds considerable promise as an interventional strategy. Beyond confirming the central role of *TP53* in sepsis-associated ferroptosis, the study is the first to propose HSYA as a potential *TP53* inhibitor for the treatment of sepsis-induced organ dysfunction.

Ethics Statement and Consent to Participate

The data used in this study were obtained from the NCBI Gene database (https://www.ncbi.nlm.nih.gov/gene/), a publicly available repository of gene-specific information that complies with international data sharing standards. All data in NCBI Gene have been de-identified and processed in accordance with ethical guidelines for public genetic data, and no individual-level identifiable information was accessed or used in this study.Since this research solely relied on publicly accessible secondary data and did not involve the collection, use, or interaction with human participants, animals, or biological specimens, no ethical approval or informed consent was required in accordance with the regulations of the Declaration of Helsinki.According to item 3 of Article 32 of the "Notice on Issuing the Measures for Ethical Review of Human-Related Life Science and Medical Research" (Guo Wei Ke Jiao Fa (2023) No. 4), research conducted using anonymized information and data may be exempted from ethical review.

Experimental research complies with relevant institutional, national, and international guidelines and legislation. Animal treatment and maintenance were carried out in strict compliance with the "Institutional Guide for the Care and Use of Laboratory Animals" guidelines. The animal study was sourced from the Animal Experimentation Center of the Army Specialty Medical Center (Animal Production License No. SCXK (Yu) 2022-0011 and an Animal Use License No. SYXK (Yu) 2022-0018). The study received approval from the Ethics Committee for Animal Experimentation of the Army Military Medical University (Ethics Approval No. AMUWE20257048).

Author Contributions

All authors made a significant contribution to the work reported, whether that is in the conception, study design, execution, acquisition of data, analysis and interpretation, or in all these areas; took part in drafting, revising or critically reviewing the article; gave final approval of the version to be published; have agreed on the journal to which the article has been submitted; and agree to be accountable for all aspects of the work.

Funding

This work was supported by Chongqing Medical Key Discipline Development Project (No.zdxk202102) and Research and application of critical care techniques for acute respiratory infectious diseases (CSTC2021jscx-gksb-N0007).

Disclosure

The authors report no conflicts of interest in this work.

References

1. Rudd KE, Johnson SC, Agesa KM, et al. Global, regional, and national sepsis incidence and mortality, 1990-2017: analysis for the global burden of disease study. *Lancet*. 2020;395(10219):200–211. doi:10.1016/S0140-6736(19)32989-7
2. Vincent JL, Jones G, David S, et al. Frequency and mortality of septic shock in Europe and North America: a systematic review and meta-analysis. *Critical Care*. 2019;23(1):196. doi:10.1186/s13054-019-2478-6
3. Tirupakuzhi Vijayaraghavan BK, Adhikari NKJ. Sepsis epidemiology and outcomes in Asia: advancing the needle. *Am J Respir Crit Care Med*. 2022;206(9):1059–1060. doi:10.1164/rccm.202207-1257ED
4. Liu L, Yue Q, Chen J, et al. Intestinal injury signaling pathway in sepsis. *Front Immunol*. 2025;16:1620965. doi:10.3389/fimmu.2025.1620965
5. Wang Y, Wang W, Zhang Y, et al. Targeting ferroptosis offers therapy choice in sepsis-associated acute lung injury. *Eur J Med Chem*. 2025;283:117152. doi:10.1016/j.ejmech.2024.117152
6. Cecconi M, Evans L, Levy M, et al. Sepsis and septic shock. *Lancet*. 2018;392(10141):75–87. doi:10.1016/S0140-6736(18)30696-2
7. Wang J, Xue X, Zhao X, et al. Forsythiaside A alleviates acute lung injury by inhibiting inflammation and epithelial barrier damages in lung and colon through PPAR-γ/RXR-α complex. *J Adv Res*. 2024;60:183–200. doi:10.1016/j.jare.2023.08.006
8. Melo-González F, Sepúlveda-Alfaro J, Schultz BM, et al. Distal consequences of mucosal infections in intestinal and lung inflammation. *Front Immunol*. 2022;13:877533. doi:10.3389/fimmu.2022.877533
9. Di Vincenzo F, Del Gaudio A, Petito V, et al. Gut microbiota, intestinal permeability, and systemic inflammation: a narrative review. *Int Emerg Med*. 2024;19(2):275–293. doi:10.1007/s11739-023-03374-w
10. Kobritz M, Nofi C, Sfakianos M, et al. Targeting sting to reduce sepsis-induced acute intestinal injury. *Surgery*. 2023;174(4):1071–1077. doi:10.1016/j.surg.2023.06.032
11. Meng M, Klingensmith NJ, Liang Z, et al. Regulators of intestinal epithelial migration in sepsis. *Shock*. 2019;51(1):88–96. doi:10.1097/SHK.0000000000001117
12. Otani S, Coopersmith CM. Gut integrity in critical illness. *J Intens Care*. 2019;7:17. doi:10.1186/s40560-019-0372-6
13. Li W, Li D, Chen Y, et al. Classic signaling pathways in alveolar injury and repair involved in sepsis-induced ALI/ARDS: new research progress and prospect. *Dis Markers*. 2022;2022:6362344. doi:10.1155/2022/6362344
14. Cicchinelli S, Pignataro G, Gemma S, et al. PAMPs and DAMPs in sepsis: a review of their molecular features and potential clinical implications. *Int J Mol Sci*. 2024;25(2):962. doi:10.3390/ijms25020962
15. Zhang H, Ma J, Hou C, et al. A ROS-mediated oxidation-O-GlcNAcylation cascade governs ferroptosis. *Nat Cell Biol*. 2025;27:1288–1300. doi:10.1038/s41556-025-01722-w
16. Shi S, Zhu C, Shi S, et al. Human spindle-shaped urine-derived stem cell exosomes alleviate severe fatty liver ischemia-reperfusion injury by inhibiting ferroptosis via GPX4. *Stem Cell Res Ther*. 2025;16(1):81. doi:10.1186/s13287-025-04202-y
17. Mo Q, Qiu Y, Liang Y, et al. Exploring long noncoding RNAs and ferroptosis in cancer progression. *Life Conflux*. 2025;1(2):e128. doi:10.71321/jjrzya36
18. Tang L, He D, Wan P, et al. Maresin-1 alleviates sepsis-induced acute kidney injury by inhibiting ferroptosis via the Nrf2/HO-1/Gpx4 signaling pathway. *Renal Failure*. 2025;47(1):2575112. doi:10.1080/0886022X.2025.2575112
19. Xi L, Gy Z, Guo R, et al. Ferroptosis in sepsis: the mechanism, the role and the therapeutic potential. *Front Immunol*. 2022;13:956361. doi:10.3389/fimmu.2022.956361
20. Zhang J, Zheng Y, Wang Y, et al. YAP1 alleviates sepsis-induced acute lung injury via inhibiting ferritinophagy-mediated ferroptosis. *Front Immunol*. 2022;13:884362. doi:10.3389/fimmu.2022.884362
21. Wang Y, Chen D, Xie H, et al. AUF1 protects against ferroptosis to alleviate sepsis-induced acute lung injury by regulating NRF2 and ATF3. *Cell Mol Life Sci*. 2022;79(5):228. doi:10.1007/s00018-022-04248-8
22. Amaral EP, Costa DL, Namasivayam S, et al. A major role for ferroptosis in mycobacterium tuberculosis-induced cell death and tissue necrosis. *J Exp Med*. 2019;216(3):556–570. doi:10.1084/jem.20181776
23. Dar HH, Tyurina YY, Mikulska-Ruminska K, et al. Pseudomonas aeruginosa utilizes host polyunsaturated phosphatidylethanolamines to trigger theft-ferroptosis in bronchial epithelium. *J Clin Invest*. 2018;128(10):4639–4653. doi:10.1172/JCI99490
24. Wang MP, Joshua B, Jin NY, et al. Ferroptosis in viral infection: the unexplored possibility. *Acta Pharmacol Sin*. 2022;43(8):1905–1915. doi:10.1038/s41401-021-00814-1
25. Chen X, Kang R, Kroemer G, et al. Ferroptosis in infection, inflammation, and immunity. *J Exp Med*. 2021;218(6). doi:10.1084/jem.20210518
26. Zhang N, Cheng C, Olaleye OE, et al. Pharmacokinetics-based identification of potential therapeutic phthalides from xuebijing, a chinese herbal injection used in sepsis management. *Drug Metabol Disposit*. 2018;46(6):823–834. doi:10.1124/dmd.117.079673
27. Cheng C, Ren C, Li Z, et al. Pharmacologically significant constituents collectively responsible for anti-sepsis action of XueBiJing, a Chinese herb-based intravenous formulation. *Acta Pharmacol Sin*. 2024;45(5):1077–1092. doi:10.1038/s41401-023-01224-1
28. Liu S, Yao C, Xie J, et al. Effect of an herbal-based injection on 28-day mortality in patients with sepsis: the EXIT-SEP randomized clinical trial. *JAMA Intern Med*. 2023;183(7):647–655. doi:10.1001/jamainternmed.2023.0780
29. Zou F, Zou J, Du Q, et al. XueBiJing injection improves the symptoms of sepsis-induced acute lung injury by mitigating oxidative stress and ferroptosis. *J Ethnopharmacol*. 2025;337(Pt 1):118732. doi:10.1016/j.jep.2024.118732
30. Bai X, Wang WX, Fu RJ, et al. Therapeutic potential of hydroxysafflor yellow a on cardio-cerebrovascular diseases. *Front Pharmacol*. 2020;11:01265. doi:10.3389/fphar.2020.01265
31. Wang YP, Guo Y, Wen PS, et al. Three ingredients of safflower alleviate acute lung injury and inhibit NET release induced by lipopolysaccharide. *Media Inflamm*. 2020;2020:2720369. doi:10.1155/2020/2720369
32. Ge C, Peng Y, Li J, et al. Hydroxysafflor yellow a alleviates acute myocardial ischemia/reperfusion injury in mice by inhibiting ferroptosis via the activation of the HIF-1α/SLC7A11/GPX4 signaling pathway. *Nutrients*. 2023;15(15):3411. doi:10.3390/nu15153411
33. He J, He M, YANG P, et al. Activation of SIRT1 by hydroxysafflor yellow a attenuates chronic unpredictable mild stress-induced microglia activation and iron death in depressed rats. *Brain Behav*. 2025;15(3):e70385. doi:10.1002/brb3.70385
34. Evans L, Rhodes A, Alhazzani W, et al. Surviving sepsis campaign: international guidelines for management of sepsis and septic shock 2021. *Crit Care Med*. 2021;49(11):e1063–e143.

35. De Freitas Caires N, Gaudet A, Portier L, et al. Endocan, sepsis, pneumonia, and acute respiratory distress syndrome. *Critical Care*. 2018;22(1):280. doi:10.1186/s13054-018-2222-7
36. Zarbock A, Nadim MK, Pickkers P, et al. Sepsis-associated acute kidney injury: consensus report of the 28th acute disease quality initiative workgroup. *Nat Rev Nephrol*. 2023;19(6):401–417. doi:10.1038/s41581-023-00683-3
37. Sun S, Duan Z, Wang X, et al. Neutrophil extracellular traps impair intestinal barrier functions in sepsis by regulating TLR9-mediated endoplasmic reticulum stress pathway. *Cell Death Dis*. 2021;12(6):606. doi:10.1038/s41419-021-03896-1
38. Smith JA, Mayeux PR, Schnellmann RG. Delayed mitogen-activated protein kinase/extracellular signal-regulated kinase inhibition by trametinib attenuates systemic inflammatory responses and multiple organ injury in murine sepsis. *Crit Care Med*. 2016;44(8):e711–20. doi:10.1097/CCM.0000000000001672
39. Vincent JL. Current sepsis therapeutics. *EBioMedicine*. 2022;86:104318. doi:10.1016/j.ebiom.2022.104318
40. Prescott HC, Angus DC. Postsepsis Morbidity. *JAMA*. 2018;319(1):91. doi:10.1001/jama.2017.19809
41. Zhang P, Liu W, Wang S, et al. Ferroptosisand its role in the treatment of sepsis-related organ injury: mechanisms and potential therapeutic approaches. *Infect Drug Resist*. 2024;17:5715–5727. doi:10.2147/IDR.S496568
42. Wang Y, Wang T, Xiang Q, et al. GPR116 promotes ferroptosis in sepsis-induced liver injury by suppressing system Xc(-)/GSH/GPX4. *Cell Biol Toxicol*. 2023;39(6):3015–3030. doi:10.1007/s10565-023-09815-8
43. Wang J, Zhu Q, Wang Y, et al. Irisin protects against sepsis-associated encephalopathy by suppressing ferroptosis via activation of the Nrf2/GPX4 signal axis. *Free Radic Biol Med*. 2022;187:171–184. doi:10.1016/j.freeradbiomed.2022.05.023
44. Guo L, Li P, Wang Y, et al. Yiqifumai injection ameliorated sepsis-induced cardiomyopathy by inhibition of ferroptosis Via Xct/Gpx4 axis. *Shock*. 2024;61(4):638–645. doi:10.1097/SHK.0000000000002257
45. Downer EJ, Gowran A, Murphy AC, et al. The tumour suppressor protein, p53, is involved in the activation of the apoptotic cascade by Delta9-tetrahydrocannabinol in cultured cortical neurons. *Eur J Pharmacol*. 2007;564(1–3):57–65. doi:10.1016/j.ejphar.2007.02.025
46. Liu Y, Su Z, Tavana O, et al. Understanding the complexity of p53 in a new era of tumor suppression. *Cancer Cell*. 2024;42(6):946–967. doi:10.1016/j.ccell.2024.04.009
47. Wang Y, Chi Y, Zhu C, et al. A novel anoikis-related gene signature predicts prognosis in patients with sepsis and reveals immune infiltration. *Sci Rep*. 2024;14(1):2313. doi:10.1038/s41598-024-52742-9
48. Wang M, Attardi LD. A balancing act: p53 activity from tumor suppression to pathology and therapeutic implications. *Ann Rev Patholog*. 2022;17:205–226. doi:10.1146/annurev-pathol-042320-025840
49. Liu Y, Gu W. p53 in ferroptosis regulation: the new weapon for the old guardian. *Cell Death Differ*. 2022;29(5):895–910. doi:10.1038/s41418-022-00943-y
50. Chen D, Chu B, Yang X, et al. iPLA2β-mediated lipid detoxification controls p53-driven ferroptosis independent of GPX4. *Nat Commun*. 2021;12(1):3644. doi:10.1038/s41467-021-23902-6
51. Kim KY, Kang YM, Lee A, et al. Hydroethanolic extract of lepidium apetalum willdenow alleviates dextran sulfate sodium-induced colitis by enhancing intestinal barrier integrity and inhibiting oxidative stress and inflammasome activation. *Antioxidants*. 2024;13(7):795. doi:10.3390/antiox13070795
52. Chen R, Cao C, Liu H, et al. Macrophage Sprouty4 deficiency diminishes sepsis-induced acute lung injury in mice [J]. *Redox Biol*. 2022;58:102513. doi:10.1016/j.redox.2022.102513
53. Otani S, Oami T, Yoseph BP, et al. Overexpression of BCL-2 in the intestinal epithelium prevents sepsis-induced gut barrier dysfunction via altering tight junction protein expression. *Shock*. 2020;54(3):330–336. doi:10.1097/SHK.0000000000001463
54. Xie B, Wang M, Zhang X, et al. Gut-derived memory γδ T17 cells exacerbate sepsis-induced acute lung injury in mice. *Nat Commun*. 2024;15(1):6737. doi:10.1038/s41467-024-51209-9
55. Zhu J, Huang Z, Lin Y, et al. Intestinal-pulmonary axis: a 'force for good' against respiratory viral infections. *Front Immunol*. 2025;16:1534241. doi:10.3389/fimmu.2025.1534241
56. Qi Y, Zhang C, Wu D, et al. Indole-3-carbinol stabilizes p53 to induce miR-34a, which targets LDHA to block aerobic glycolysis in liver cancer cells. *Pharmaceuticals*. 2022;15(10):1257. doi:10.3390/ph15101257
57. Yu Z, Wang H, Fang Y, et al. Molecular chaperone HspB2 inhibited pancreatic cancer cell proliferation via activating p53 downstream gene RPRM, BAI1, and TSAP6. *J Cell Biochem*. 2020;121(3):2318–2329. doi:10.1002/jcb.29455
58. Zhang H, Liu J, Zhou Y, et al. Neutrophil extracellular traps mediate m(6)A modification and regulates sepsis-associated acute lung injury by activating ferroptosis in alveolar epithelial cells. *Int J Bio Sci*. 2022;18(8):3337–3357. doi:10.7150/ijbs.69141
59. Sun JK, Huangfu XT, Yin X, et al. Ferroptosis is involved in the IL-9-induced intestinal barrier injury in sepsis: an experimental animal and translational study. *Int J Surg*. 2025;111:4314–4324. doi:10.1097/JS9.0000000000002541
60. Jing X, Chen Z, Zhang M, et al. Melatonin mitigates the lipopolysaccharide-induced myocardial injury in rats by blocking the p53/xCT pathway-mediated ferroptosis. *Naunyn-Schmiedeberg's Arch Pharmacol*. 2025;398(2):1653–1663. doi:10.1007/s00210-024-03367-2
61. Sun M, Li J, Mao L, et al. p53 deacetylation alleviates sepsis-induced acute kidney injury by promoting autophagy. *Front Immunol*. 2021;12:685523. doi:10.3389/fimmu.2021.685523
62. Xie L, Zhang G, Wu Y, et al. Protective effects of Wenqingyin on sepsis-induced acute lung injury through regulation of the receptor for advanced glycation end products pathway. *Phytomedicine*. 2024;129:155654. doi:10.1016/j.phymed.2024.155654
63. Koppula P, Zhuang L, Gan B. Cystine transporter SLC7A11/xCT in cancer: ferroptosis, nutrient dependency, and cancer therapy. *Proteincell*. 2021;12(8):599–620. doi:10.1007/s13238-020-00789-5
64. Pasino M, Speciale A, Ravera S, et al. Targeting the p53/xCT/GSH Axis with PRIMA-1(Met) combined with sulfasalazine shows therapeutic potential in chronic lymphocytic leukemia. *Int J Mol Sci*. 2025;26(12):5559. doi:10.3390/ijms26125559
65. Hu T. Xuebijing injection for sepsis treatment: when will it be approved outside of China? *JAMA Intern Med*. 2023;183(11):1280–1281. doi:10.1001/jamainternmed.2023.4398
66. Xue X, Deng Y, Wang J, et al. Hydroxysafflor yellow A, a natural compound from carthamus tinctorius L with good effect of alleviating atherosclerosis. *Phytomedicine*. 2021;91:153694. doi:10.1016/j.phymed.2021.153694
67. Chen J, Ren C, Yao C, et al. Identification of the natural chalcone glycoside hydroxysafflor yellow A as a suppressor of P53 overactivation-associated hematopoietic defects. *MedComm*. 2023;4(5):e352. doi:10.1002/mco2.352
68. Wang XT, Peng Z, An Y, et al. Paeoniflorin and hydroxysafflor yellow a in xuebijing injection attenuate sepsis-induced cardiac dysfunction and inhibit proinflammatory cytokine production. *Front Pharmacol*. 2020;11:614024. doi:10.3389/fphar.2020.614024